FWI inversion sensitivities of the elastic stiffness coefficients in fractured media: analytic results

Wenyong Pan, Kris Innanen, Mike Fehler, Gary Margrave, Xinding Fang

ABSTRACT

Full waveform inversion (FWI) is very powerful in estimating the subsurface properties by minimizing the difference between the modelled data and observed data iteratively. Multi-parameter FWI can also be employed to inverse the properties of the naturally fractured reservoirs, when assuming that the wavelength is much larger than the fracture size. Estimating the fracture properties using multi-parameter FWI will be challenging for several difficulties, one of which is the cross-talk problem in multi-parameter FWI. And it refers to that the seismic wavefields responses by different parameters' perturbations are coupled together. This difficulty also gives rise to the parameterization issue for multi-parameter FWI. The Fréchet derivative serves as the inversion sensitivity for the least-squares inverse problem and it is interpreted as the seismic wavefields response corresponding to the model parameter's perturbation. Furthermore, the Fréchet derivative control the trade-off among different parameters and the amplitude variations with varying the scattering angle and azimuthal angle (in 3D) (radiation pattern) can help identify the efficiency of the parameterization and design optimal acquisition geometry. In this research, we focus on studying the inversion sensitivities of elastic constants in fractured media (parallel vertical fractures and orthorhombic fractures). The inversion sensitivity can be described using scattering patterns with varying the scattering angle and azimuth angle. We, first, review the general principle of FWI and explain the angle dependence nature of the inversion sensitivity. Then, we give the explicit Fréchet derivative for the general anisotropic media with Born approximation and reproduce the scattering patterns by a local isotropic inclusion. The 3D Fréchet derivative with respect to different elastic constants for parallel vertical fractured media (described as HTI model) are provided. And then, we analyze the scattering characteristics due to the fractured inclusion and discuss the inversion sensitivities with varying the scattering angle and azimuthal angle. Finally, we give the scattering patterns with respect to the elastic constants in orthorhombic fractured media and analyze the FWI inversion sensitivities for these elastic stiffness coefficients.

INTRODUCTION

Naturally fractured reservoirs are commonly existed in subsurface and they play important role in present hydrocarbon production (Nelson, 1985). The properties of the fractures (e.g., fracture orientation and intensity) are extremely valuable for reservoir characterization. To obtain effective parameters of the cracked media, the finite fracture spacings and their detailed spatial distributions can be neglected and the fractured rock can be considered as equivalent anisotropic solids with long wavelength approximation.

The reflection seismic signatures from anisotropic fractures can be described by stiffness coefficients c_{ij} (or compliances s_{ij}) (Hudson, 1981; Schoenberg, 1983) or the Thomsen-type parameters (ε, δ and γ) introduced by Thomsen (1986) for transverse isotropy with vertical symmetry axis (VTI media). And for transverse isotropy with horizontal symmetry axis (HTI media), the simplest azimuthal anisotropic model for describing the vertical cracks, the reflection seismic signatures can also be described by the Thomsen-type coefficients (Rüger, 1997; Tsvankin, 1997b).

While most of the present studies for fracture properties estimation from surface measurements are mainly performed by Amplitude Variations versus Offset (AVO) and Azimuth (AVAZ) analysis (Tsvankin, 1997b; Bakulin et al., 2000; Tsvankin, 2001; Tsvankin and Grechka, 2011; Mahmoudian, 2013). And the measured phase velocity and normal-moveout (NMO) velocity are always used to estimate the stiffness coefficients (Vestrum, 1994) or Thomsen's parameters (Tsvankin, 1997b). However, the AVO/AVAZ analysis is based on the assumption that the subsurface reflector is laterally invariant. The application of this technique for fracture properties inversion in laterally variant area renders the accuracy of the inversion results to be questionable (Bansal and Sen, 2010).

In recent years, full waveform inversion (FWI) method becomes popular for estimating the subsurface parameters. FWI employs full wavefields information to estimate subsurface properties through an iterative process by minimizing the difference between the observed data and synthetic data (Tarantola and Valette, 1982; Pratt et al., 1998; Virieux and Operto, 2009). It can provide more diagnostic information and offers far greater resolving capability (Zhou and Greenhalgh, 2009). The gradient in FWI can be constructed by convolution between the Fréchet derivative (or first order partial derivative wavefields) and the complex conjugate of the data residuals. An adjoint state method based on Born approximation is always employed to calculate the gradient for avoiding the direct computation of the partial derivative wavefields (Liu and Tromp, 2006), which is equivalent to a reverse time migration process. Furthermore, the approximate Hessian matrix used in Gauss-Newton FWI (Pratt et al., 1998; Pan et al., 2014) is also constructed by two partial derivative wavefields. Hence, the Fréchet derivative can be interpreted as the wavefields changes corresponding the perturbations of the model parameters(e.g., density, elastic constants or Thomsen's parameters) and they serve as sensitivity kernels in least-squares inverse problem.

Estimating the seismic wavefields response corresponding to the perturbations of the model parameters is a classical inverse problem of exploration geophysics. And many researchers have concentrated on using these kernels for sensitivity analysis and seismic waveform tomography in anisotropic media (Chapman and Coates, 1994; Tromp et al., 2005; Liu and Tromp, 2006). Calvet et al. (2006) gave the 3D Fréchet derivative for P-wave travel time in VTI medium with far-field approximation of the Green's tensor. Zhou and Greenhalgh (2009) formulated the explicit expressions for 3D Fréchet derivative in a general anisotropic medium. Moreover, the Fréchet derivative with Born approximation can be used to derive the linearized reflection coefficients for AVO/AVAZ analysis (Shaw and K.Sen, 2004; Tsvankin, 1995).

Fracture properties estimation using multi-parameter full waveform inversion method is challenging. This is because the wavefields responses corresponding to different parameters' perturbations are coupled together, which is referred as the trade-off or cross-talk between the parameters (Tarantola, 1986; Gholami et al., 2013b,a; Operto et al., 2013; Oh and Min, 2014; Alkhalifah and Plessix, 2014). This difficulty raises the parameterization issue for multi-parameter FWI and proper parameterization for multi-parameter FWI should be determined to avoid the over the parameterization of the optimization problem and provide a reliable inversion process. The Fréchet derivative, namely radiation pattern (scattering pattern), control the trade-off between the parameters. The amplitude variation of the sensitivity kernel with the scattering angle gives insights of the wavefields response to the parameter's perturbation and reveals the intrinsic relationship between seismic AVO and FWI (Stolt and Weglein, 2012; Innanen, 2014). Studying the sensitivity kernels for different parameters can help select appropriate parameterization for multi-parameter FWI (Eaton, 1991) and design optimal acquisition geometry(Gholami, 2012; Plessix and Cao, 2011).

Wu and Aki (1985b,a) and Sato and Fehler (1997) discussed the elastic scattering patterns due to a general elastic heterogeneity in the low-frequency range (Rayleigh scattering). Tarantola (1986) originally involved the radiation patterns for sensitivity analysis of different parameter classes and gave a strategy for nonlinear elastic inversion of seismic reflection data. Gholami (2012) assessed the sensitivity of the seismic data to different data parameterizations of acoustic VTI media. And they also showed that the acquisition geometry controls the resolving power of multi-parameter FWI and wide-aperture acquisition geometry is more flexible for determining suitable parameterization.

The majority of the existing studies for fracture properties estimation mainly focus on HTI media (Rüger, 1997; Contreras et al., 1999; Bakulin et al., 2000; Zheng et al., 2013), the simplest effective model for describing the fractured reservoirs. The HTI model with single fracture system is actually a degenerated case of an orthorhombic symmetry, which is also commonly existed in naturally fractured reservoirs(Wild and Crampin, 1991; Schoenberg and Helbig, 1997; Tsvankin, 1997a). The difficulties in dealing with the 9 independent elastic constants in orthorhombic fracture preclude this model from application in exploration geophysics. The forward modeling problem for orthorhombic media has been studied by many researchers (Tsvankin and Chesnokov, 1990; Brown et al., 1991; Song and Alkhalifah, 2013), while the inverse problem for orthorhombic fractured media has rarely been investigated, especially using full waveform inversion method. In this research, following Ben-Menahem and Singh (1981) and Ben-Menahem et al. (1991)'s method, we provide the explicit expressions for Fréchet derivative in orthorhombic media with respect to different elastic constants. The radiation patterns are derived within spherical coordinates and they serve as the basis and inversion engines for estimating the fracture properties using multi-parameter FWI strategy.

FWI INVERSION SENSITIVITY

General Principle of FWI

Full waveform inversion (FWI) estimates the subsurface parameters through an iterative process by minimizing the difference between the synthetic data **Bu** and observed data **d** (Tarantola, 1984). The misfit function Φ is formulated in a least-squares form (Virieux and Operto, 2009):

$$\Phi = \frac{1}{2}\|\mathbf{d} - \mathbf{B}\mathbf{u}\|^2, \tag{1}$$

where $\mathbf{B}$ is the forward modeling operator, $\mathbf{u}$ mean the wavefields and $\|\cdot\|^2$ means the ℓ-2 norm. The minimum value of the misfit function is sought in the vicinity of the starting model $m_0(\mathbf{r})$ and the updated model can be written as the summation of the starting model and a model perturbation $\delta m(\mathbf{r})$.

$$m_{k+1}(\mathbf{r}) = m_k(\mathbf{r}) + \mu_k \delta m_k(\mathbf{r}), \tag{2}$$

where k indicates the number of iteration, μ_k is the step length, a scalar constant used to scale the model perturbation $\delta m_k(\mathbf{r})$ and it can be obtained through a line search method. The model perturbation can be expressed as:

$$\delta m = -H^{-1} g, \tag{3}$$

where g is the gradient, the first order partial derivative of the misfit function with respect to the model parameters. And it can be constructed by a convolution between the first order partial derivative wavefields and complex conjugate of the data residuals:

$$g = \frac{\partial \Phi}{\partial m} = \frac{\partial \mathbf{u}}{\partial m} \Delta \mathbf{d}^{\dagger}, \tag{4}$$

where $\frac{\partial \mathbf{u}}{\partial m}$ is known as the Fréchet derivative (or sensitive matrix), $\Delta \mathbf{d}$ indicate the data residuals and the symbol $'\dagger'$ means complex conjugate. And H is the Hessian matrix, the second order partial derivative of the misfit function with respect to the model parameters. In Gauss-Newton method, the approximate Hessian matrix can be written as the auto-correlation of two partial derivative wavefields:

$$H_a = \left[\frac{\partial \mathbf{u}}{\partial m}\right]^{\dagger} \left[\frac{\partial \mathbf{u}}{\partial m}\right]. \tag{5}$$

FRÉCHET DERIVATIVE IN GENERAL ANISOTROPIC MEDIA WITH BORN APPROXIMATION

The equation of motion in general anisotropic and elastic media can be written as follows (Wu and Aki, 1985b; Ben-Menahem and Jr, 1990; Gibson-Jr, 1991; Zhou and Greenhalgh, 2009; Aki and Richards, 2002):

$$\frac{\partial \sigma_{ij}}{\partial x_j} + f_i = \rho \frac{\partial^2 u_i}{\partial t^2}, \tag{6}$$

where $\mathbf{u}\left(\mathbf{r}, t\right)$ indicates the displacement vector at Cartesian coordinate position $\mathbf{r}(x, y, z)$ and time t. $\mathbf{f}\left(\mathbf{r}_s\right)$ is the force term at position $\mathbf{r}_s$, ρ is the density and σ_{ij} denotes the stress tensor, which can be defined using Hooke's law:

$$\sigma_{ij} = c_{ijkl} \frac{\partial u_k}{\partial x_l}, \tag{7}$$

where c_{ijkl} indicates the elastic modulus tensor and the subscripts i, j, k and l take on the values of 1, 2, 3 (or x, y, z). The solution of equation (6) can be obtained using the integral form of the Green's tensor vector in frequency domain (Ben-Menahem and Singh, 1981; Kamath and Tsvankin, 2014):

$$\bar{u}_i\left(\mathbf{r},\omega\right) = \int_{\Omega(\mathbf{r}_s)} \int_{\omega_s} f_j(\mathbf{r}_s,\omega_s) G_{ij}(\mathbf{r},\omega;\mathbf{r}_s,\omega_s) d\Omega(\mathbf{r}_s) d\omega_s, \tag{8}$$

where $G_{ij}(\mathbf{r},\omega;\mathbf{r}_s,t_s)$ indicates the i component of the Green's tensor vector at position $\mathbf{r}$ due to a point source $f_j(\mathbf{r}_s,\omega_s)$ in j direction at position $\mathbf{r}_s$. And $\Omega\left(\mathbf{r}_s\right)$ indicates the volume including all of the sources.

Considering that a general anisotropic inclusion with density ρ and elastic constants c_{ijkl} is embedded in an infinite isotropic elastic background with properties $\tilde{\rho}$ and $\tilde{c}_{ijkl}$. Here, we define the scattering potentials $\delta\rho$ and δc_{ijkl} as the differences between the perturbed and unperturbed model properties (Stolt and Weglein, 2012):

$$\begin{aligned} \delta\rho &= \rho - \tilde{\rho}, \\ \delta c_{ijkl} &= c_{ijkl} - \tilde{c}_{ijkl}, \end{aligned} \tag{9}$$

where $\delta\rho$ and δc_{ijkl} denote the density and elastic constants perturbations. Assuming that the size of the anisotropic obstacle is rather small compared to the wavelength of the incident wave, the perturbed wavefields corresponding these model variations can be obtained as:

$$\delta\mathbf{u} = \mathbf{u} - \tilde{\mathbf{u}}, \tag{10}$$

where $\tilde{\mathbf{u}}$ and $\delta\mathbf{u}$ indicate the unperturbed wavefields and scattered wavefields respectively. Plugging equations (9) and (10) into equation (6), we can ignore the high order terms based on Born approximation and the equation of motion splits into two equations:

$$\frac{\partial}{\partial x_j}\left(\tilde{c}_{ijkl}\frac{\partial \tilde{u}_k}{\partial x_l}\right) - \tilde{\rho}\frac{\partial^2 \tilde{u}_i}{\partial t^2} = -f_i, \tag{11}$$

$$\frac{\partial}{\partial x_j}\left(\tilde{c}_{ijkl}\frac{\partial \delta u_k}{\partial x_l}\right) - \tilde{\rho}\frac{\partial^2 \delta u_i}{\partial t^2} = \delta\rho\frac{\partial^2 \tilde{u}_i}{\partial t^2} - \frac{\partial \delta M_{ij}}{\partial x_j}, \tag{12}$$

where $\delta\mathbf{M}$ in equation (12) can be considered as the equivalent moment tensor source and it corresponds to the perturbations of the elastic constants:

$$\delta M_{ij} = \delta c_{ijkl}\frac{\partial \tilde{u}_k}{\partial x_l}. \tag{13}$$

We notice, first, that equation (11) is equivalent to equation (6), meaning that the unperturbed wavefield $\tilde{\mathbf{u}}$ propagates in the isotropic background media. Further examination reveals that equation (12) describes the propagation of the scattered wavefield $\delta\mathbf{u}$ in the isotropic background media. The right hand side of the equation (12) is always referred to as "scattered sources" or "secondary Born sources". It underlines the fact that the scattered wavefields due to the perturbations in the model parameters such as density $\delta\rho$ or elastic coefficients δc_{ijkl}, can be interpreted as the wavefields generated by a set of secondary body forces, which propagate in the current, unperturbed medium (Dietrich and Kormendi, 1990).

According to equation (8), the solution of equation (12) can be written as an integral formulation in frequency domain:

$$\begin{aligned}\delta\bar{u}_n(\mathbf{r},\omega) = &\int_{\Omega(\mathbf{r}')}\int_{\omega'} \delta\rho\omega^2\tilde{u}_i\tilde{G}_{ni}(\mathbf{r},\omega;\mathbf{r}',\omega')d\Omega(\mathbf{r}')d\omega' \\ &+ \int_{\Omega(\mathbf{r}')}\int_{\omega'} \frac{\partial\delta M_{ij}}{\partial x'_j}\tilde{G}_{ni}(\mathbf{r},\omega;\mathbf{r}',\omega')d\Omega(\mathbf{r}')d\omega',\end{aligned} \tag{14}$$

where $\tilde{G}_{ij}(\mathbf{r},\omega;\mathbf{r}',\omega')$ indicates the Green's tensor in the unperturbed background medium due to the scattering source at position $\mathbf{r}' = (x', y', z')$. Ignoring the contribution from density (Here, we only consider the perturbations of the elastic constants) and applying integration by parts with far-field approximation, the scattered wavefields can be obtained as:

$$\delta\bar{u}_n(\mathbf{r},\omega) \approx -\int_{\Omega(\mathbf{r}')}\int_{\omega'} \delta M_{ij}\frac{\partial\tilde{G}_{ni}(\mathbf{r},\omega;\mathbf{r}',\omega')}{\partial x'_j}d\Omega(\mathbf{r}')d\omega'. \tag{15}$$

or an compact form:

$$\delta\bar{u}_n \approx -\delta M_{ij}\tilde{G}_{ni,j}. \tag{16}$$

Taking partial derivative of the scattered wavefields with respect to the variations of the model parameters yields the Fréchet derivative for a general anisotropic media:

$$\frac{\delta\bar{u}_n(\mathbf{r},\omega)}{\partial m} = -\int_{\Omega(\mathbf{r}')}\int_{\omega'} \frac{\partial\delta M_{ij}}{\partial m}\frac{\partial\tilde{G}_{ni}(\mathbf{r},\omega;\mathbf{r}',\omega')}{\partial x'_j}d\Omega(\mathbf{r}')d\omega', \tag{17}$$

where m denotes elastic constants c_{ijkl} for a general anisotropic medium. Equation (17) is known as the Fréchet derivative (or inversion sensitivity kernel) which is widely analyzed and utilized in the linearized inversion framework, such as full waveform inversion (Tarantola and Valette, 1982; Tarantola, 1984, 1986; Pratt et al., 1998; Virieux and Operto, 2009).

MOMENT TENSOR SOURCES AND RADIATION PATTERNS

In the above section, we give the explicit expressions of the Fréchet derivative for a general anisotropic media. In this section, firstly, we will review the Geen's tensor in isotropic homogeneous media with far-field approximation and the source radiation patterns with the moment tensor source. And then we will explain how to describe the Fréchet derivative using the scattering patterns due to the model parameters' perturbations.

Green's Tensor in Isotropic Elastic Media

In order to obtain the scattered wavefields in equation (14) and the Fréchet derivative shown in equation (17), firstly, we need get the Green's tensor in the background isotropic medium. Applying Helmholtz decomposition to the equation of motion for isotropic elastic media, the time domain Green's function obtained as (Aki and Richards, 2002; Chapman, 2004):

$$\mathbf{G}\left(\mathbf{r},t;\mathbf{r}_s,t_s\right)=\frac{\delta\left(t-r/\alpha\right)}{4\pi\rho\alpha^2 r}\hat{\mathbf{r}}\hat{\mathbf{r}}^\dagger+\frac{\delta\left(t-r/\beta\right)}{4\pi\rho\beta^2 r}\left(\mathbf{I}-\hat{\mathbf{r}}\hat{\mathbf{r}}^\dagger\right)$$
$$+\frac{\left[H\left(t-r/\alpha\right)-H\left(t-r/\beta\right)\right]}{4\pi\rho r^3}\left(3\hat{\mathbf{r}}\hat{\mathbf{r}}^\dagger-\mathbf{I}\right), \tag{18}$$

where α and β indicate the P-wave velocity and S-wave velocity, H denotes the Heaviside function and the symbol † denotes transpose operation. And **I** is the unit vector indicating the direction of source term:

$$\mathbf{I}=\hat{\mathbf{r}}\hat{\mathbf{r}}^\dagger+\hat{\theta}\hat{\theta}^\dagger+\hat{\phi}\hat{\phi}^\dagger, \tag{19}$$

where $\hat{\mathbf{r}}$, $\hat{\theta}$ and $\hat{\phi}$ are unit vectors in spherical coordinates (r,θ,ϕ):

$$\begin{aligned}\hat{\mathbf{r}}^\dagger&=\left[\sin\theta\cos\phi,\sin\theta\sin\phi,\cos\theta\right],\\ \hat{\theta}^\dagger&=\left[\cos\theta\cos\phi,\cos\theta\sin\phi,-\sin\theta\right],\\ \hat{\phi}^\dagger&=\left[-\sin\phi,\cos\phi,0\right].\end{aligned} \tag{20}$$

and θ indicates the inclination angle departs from z axis and ϕ indicates the azimuthal angle departs from x axis. Equation (18) is the dyadic Green's function, obtained by Stokes (1851) firstly. The detailed proofs can be found in Hudson (1980) and Aki and Richards (2002). We can notice that the first two terms in equation (18) decay as r^{-1}, expected as spherical spreading. While the third term decays more rapidly as r^{-3}. Hence, with far-field approximation, the near-field terms can just be ignored and the Green's tensor in frequency domain can be obtained as:

$$G_{ij}\left(\mathbf{r},\omega;\mathbf{r}_s,\omega_s\right)\approx\frac{\mathbf{exp}(-ik_\alpha r)}{4\pi\rho\alpha^2 r}\hat{r}_i\hat{r}_j+\frac{\mathbf{exp}(-ik_\beta r)}{4\pi\rho\beta^2 r}\left(\hat{\theta}_i\hat{\theta}_j+\hat{\phi}_i\hat{\phi}_j\right), \tag{21}$$

where $k_\alpha=\omega/\alpha$ and $k_\beta=\omega/\beta$ are the P-wave the S-wave wavenumber respectively.

The first term in equation (21) represents the wave motion in the direction of **r**, which corresponds to the P-wave motion. And the second and third terms describe the wave motions perpendicular to radial direction and they denote the wave motions of SV-wave SH-wave respectively. The factors $\mathbf{r}\mathbf{r}^\dagger$, $\hat{\theta}\hat{\theta}^\dagger$ and $\hat{\phi}\hat{\phi}^\dagger$ describe the radiation patterns of P-wave, SV-wave and SH-wave and the directional behaviour of the displacement magnitude.

Moment Tensor Sources and Radiation Patterns

In earthquake seismology, the moment tensors are used to describe dislocation type sources, explosive/pressure sources and higher order type of sources such as dipoles, which have been widely acknowledged in elasticity (Aki and Richards, 2002; Sato and Fehler, 1997; Karpfinger et al., 2009). The total displacement generated by the source is the summation of the displacements owing to the nine individual double forces. Thus the total displacement can be constructed by scalar product of the moment tensor and the spatial derivative of the Green's function:

$$\bar{u}_n=M_{ij}G_{ni,j}, \tag{22}$$

where the convention subscripts summation applies. The nine elements of M_{ij} constitute of the source moment tensor (Ben-Menahem and Singh, 1981) and it can be represented by a matrix **M**:

$$\mathbf{M} = \begin{bmatrix} M_{11} & M_{12} & M_{13} \\ M_{21} & M_{22} & M_{23} \\ M_{31} & M_{32} & M_{33} \end{bmatrix}. \tag{23}$$

Plugging the Green's tensor components into equation (22) yields the displacement wavefields solution:

$$\begin{aligned} \bar{u}_n(\mathbf{r},\omega) = &-\frac{i\omega\mathbf{exp}(-ik_\alpha r)}{4\pi\rho\alpha^3 r}M_{ij}R_nR_iR_j \\ &+\frac{i\omega\mathbf{exp}(-ik_\beta r)}{4\pi\rho\beta^3 r}M_{ij}\left(R_nR_i-\delta_{ni}\right)R_j, \end{aligned} \tag{24}$$

where δ_{ni} is the Kronecker delta function. The detailed instruction of derivation process can be found in Pujol (2003) and Chapman (2004). The total wavefileds **u** is the summation of P-wave, SV-wave and SH-wave wavefields and equation (24) can be written as an compact matrix form:

$$\bar{\mathbf{u}}(\mathbf{r},\omega) = -\frac{i\omega\mathbf{exp}(-ik_\varrho r)}{4\pi\rho\varrho^3 r}\hat{\mathbf{g}}\left(\hat{\mathbf{g}}^\dagger\mathbf{M}\hat{\mathbf{r}}\right), \tag{25}$$

where ϱ indicates α P-wave velocity or β for S-wave velocity and k_ϱ indicates P-wave or S-wave wavenumbers. The radiation patterns $\mathcal{R}$ for P-wave, SV-wave and SH-wave are determined by the term $\left(\hat{\mathbf{g}}^\dagger\mathbf{M}\hat{\mathbf{r}}\right)$ when $\hat{\mathbf{g}}$ is $\hat{\mathbf{r}}$, $\hat{\theta}$ or $\hat{\phi}$ respectively.

$$\mathcal{R}(\theta,\phi) = \hat{\mathbf{g}}^\dagger\mathbf{M}\hat{\mathbf{r}}. \tag{26}$$

The explicit expressions for the radiation patterns have been given by Aki and Richards (2002) and Chapman (2004). These equations allow us to construct the wavefields due to various moment tensor sources such as explosive, dipole, double-couple and etc. Here, in this section, we give two types of sources for illustration. Considering the single dipole source due to M_{33} and the double couple source due to M_{12}:

$$\mathbf{M}_D = 2\begin{bmatrix} 0 & 0 & 0 \\ 0 & 0 & 0 \\ 0 & 0 & M_{33} \end{bmatrix}, \mathbf{M}_{DC} = \begin{bmatrix} 0 & M_{12} & 0 \\ M_{21} & 0 & 0 \\ 0 & 0 & 0 \end{bmatrix}. \tag{27}$$

Submitting them into equation (26) gives the corresponding radiation patterns:

$$\boldsymbol{\mathcal{R}}_P^D(\theta,\phi) = 2\cos^2\theta, \boldsymbol{\mathcal{R}}_{SV}^D(\theta,\phi) = -\sin 2\theta, \boldsymbol{\mathcal{R}}_{SH}^D(\theta,\phi) = 0. \tag{28}$$

$$\boldsymbol{\mathcal{R}}_P^{DC} = \sin 2\phi\sin^2\theta, \boldsymbol{\mathcal{R}}_{SV}^{DC} = \tfrac{1}{2}\sin 2\phi\sin 2\theta, \boldsymbol{\mathcal{R}}_{SH}^{DC} = \cos 2\phi\sin 2\theta. \tag{29}$$

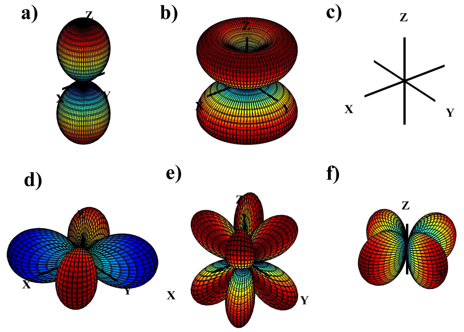

FIG. 1. (a), (b) and (c) show the radiation patterns of P-wave, SV-wave and SH-wave by a dipole source due to M_{33}. (d), (e) and (f) show the radiation patterns of P-wave, SV-wave and SH-wave due to M_{12}. Detailed instructions about the radiation patterns can be founded in Chapter 3 in Aki and Richards (2002) and Chapter 4 in Chapman (2004).

Figures 1a, b and c show the source radiation patterns of P-wave, SV-wave and SH-wave by the dipole source due to M_{33}. Figures 1d, e and f show the source radiation patterns of P-wave, SV-wave and SH-wave by the double couple source due to M_{12}. The detailed instructions can be founded in Chapman (2004).

If we ignore the contribution of density, the total scattered wavefields $\delta\bar{\mathbf{u}}$ is the solution of equation (12) by the equivalent moment tensor sources due to the perturbations of the elastic constants δc_{ijkl}. Similarly, we can obtained the scattered wavefields as:

$$\delta u_n(\mathbf{r},\omega) = -\delta M_{ij}\tilde{G}_{ni,j}, \tag{30}$$

And the elements in the equivalent moment tensor source $\delta\mathbf{M}$ can be expressed as (Musgrave, 1970):

$$\delta M_{ij} = \delta c_{ijkl}\tilde{e}_{kl}. \tag{31}$$

where $\tilde{e}_{kl} = \partial\tilde{u}_k/\partial x'_l$ is the strain tensor of the incident wavefields. Applying "Voigt recipe" to the elastic constants perturbation matrix $\delta\mathbf{c}$, equation (31) can be written in a matrix form:

$$\begin{bmatrix} \delta M_{11} \\ \delta M_{22} \\ \delta M_{33} \\ \delta M_{23} \\ \delta M_{13} \\ \delta M_{12} \end{bmatrix} = \begin{bmatrix} \delta c_{11} & \delta c_{12} & \delta c_{13} & \delta c_{14} & \delta c_{15} & \delta c_{16} \\ & \delta c_{22} & \delta c_{23} & \delta c_{24} & \delta c_{25} & \delta c_{26} \\ & & \delta c_{33} & \delta c_{34} & \delta c_{35} & \delta c_{36} \\ & & & \delta c_{44} & \delta c_{45} & \delta c_{46} \\ & & & & \delta c_{55} & \delta c_{56} \\ & & & & & \delta c_{66} \end{bmatrix} \begin{bmatrix} \tilde{e}_{11} \\ \tilde{e}_{22} \\ \tilde{e}_{33} \\ 2\tilde{e}_{23} \\ 2\tilde{e}_{13} \\ 2\tilde{e}_{12} \end{bmatrix}. \tag{32}$$

We can observe that the perturbations of different elastic constants correspond to different types of sources. For example, δc_{11}, δc_{22} and δc_{33} serve as single dipole source and δc_{44},

δc_{55} and δc_{66} serve as double couple sources. Similarly to equation (25), the scattered wavefields can be written in a compact form:

$$\delta \bar{\mathbf{u}}\left(\mathbf{r},\omega\right) = -\frac{i\omega \mathbf{exp}(-ik_{\varrho}r)}{4\pi\rho\varrho^3 r}\hat{\mathbf{g}}\left(\hat{\mathbf{g}}^{\dagger}\delta\mathbf{M}\hat{\mathbf{r}}\right), \tag{33}$$

when $\hat{\mathbf{g}}$ is $\hat{\mathbf{r}}$, $\hat{\theta}$ or $\hat{\phi}$, we can obtain the scattered P-wave, SV-wave or SH-wave wavefields respectively. And the information of incident wavefields is encoded in the equivalent moment tensor source $\delta\mathbf{M}$.

SCATTERING PATTERNS AND INVERSION SENSITIVITIES BY FRACTURED MEDIA

In this section, firstly, we will reproduce the scattering patterns caused by the local isotropic heterogeneity and explain Fréchet derivative and inversion sensitivities with respect to Lamé constants for elastic full waveform inversion. Then, we extend the theory to analyze the inversion sensitivities and scattering patterns for parallel vertical fractured media (HTI model). The scattering patterns for different elastic constants with varying scattering angle and azimuth are discussed by introducing two acquisition geometries. Finally, the inversion sensitivities for the elastic constants in orthorhombic media are derived and analyzed.

The Isotropic Case

The scattering characteristics of elastic wave due to the local elastic inhomogeneity have been studied by many researchers (Wu and Aki, 1985b,a; Sato and Fehler, 1997). Tarantola (1986) discussed the influence of different parameterizations to efficiency of elastic full waveform inversion by introducing the scattering patterns due to the parameters' perturbations. In this section, we will reproduce the 3D scattering coefficients using equation (33) and explain the Fréchet derivative with respect to Lamé constants λ and μ. The elastic constants perturbation matrix $\delta\mathbf{c}$ for the local elastic obstacle can be expressed as:

$$\delta c_{ijkl}^{\mathrm{iso}} = \delta\lambda\delta_{ij}\delta_{kl} + \delta\mu\left(\delta_{ik}\delta_{jl} + \delta_{jk}\delta_{il}\right). \tag{34}$$

Inserting it into equation (32) gives the isotropic moment tensor source:

$$\delta M_{ij}^{\mathrm{iso}} = \delta\lambda\delta_{ij}\left(\nabla\cdot\grave{\mathbf{u}}\right) + 2\delta\mu\tilde{e}_{ij}, \tag{35}$$

where $\grave{\mathbf{u}}$ denotes the incident wavefields and $\nabla\cdot\grave{\mathbf{u}} = \tilde{e}_{11} + \tilde{e}_{22} + \tilde{e}_{33}$ is the dilatation. Taking partial derivative of moment tensor source gives an explosive-type source due to perturbation of λ;

$$\frac{\partial M_{ij}^{\mathrm{iso}}}{\partial\lambda} = \left(\nabla\cdot\grave{\mathbf{u}}\right)\delta_{ij}. \tag{36}$$

To obtain the strain components of the incident wavefields, we can consider the incident plane P-wave:

$$\grave{\mathbf{u}}(\mathbf{r},t) = U\mathbf{exp}\left[i(\omega t - \mathbf{k}_{\alpha}\cdot\mathbf{n})\right]\mathbf{d}, \tag{37}$$

where U is the amplitude of the incident P-wave and $\mathbf{n} = \mathbf{x}+\mathbf{y}+\mathbf{z}$ indicates the unit vector in Cartesian coordinates. And $\mathbf{k}_{\alpha}$ is the wavenumber vector in Spherical coordinates and $\mathbf{d}$

is the polarization vector indicating the positive direction of the particle motion:

$$\begin{aligned}\mathbf{k}_\alpha &= k_\alpha \mathbf{p} \\ &= k_\alpha \left(\sin\vartheta\cos\varphi\mathbf{x} + \sin\vartheta\sin\varphi\mathbf{y} + \cos\vartheta\mathbf{z}\right),\end{aligned} \tag{38}$$

$$\mathbf{d} = \sin\vartheta\cos\varphi\mathbf{x} + \sin\vartheta\sin\varphi\mathbf{y} + \cos\vartheta\mathbf{z}, \tag{39}$$

where ϑ is the inclination angle of incident wave, which departs from z axis and φ departing from x axis indicates the azimuth angle of the incident wave. And $\mathbf{p}$ is the unit vector in Spherical coordinates. Thus, the strain components can be obtained as:

$$\tilde{e}_{ij} = -ik_\alpha U d_i p_j \mathbf{exp}\left[i(\omega t - \mathbf{k}_\alpha \cdot \mathbf{n})\right]. \tag{40}$$

Plugging equation (40) into equation (33) gives the equivalent moment tensor source δM_{ij}^{iso} for an elastic inclusion:

$$\delta M_{ij}^{iso} = \left[\delta\lambda d_i p_i \delta_{ij} + 2\delta\mu d_i p_j\right]\mathbf{F}, \tag{41}$$

where the summation applies to the subscripts of the term $d_i p_i$ and

$$\mathbf{F} = -ik_\alpha U \mathbf{exp}\left[i(\omega t - \mathbf{k}_\alpha \cdot \mathbf{n})\right].$$

Inserting equation (41) into equation (30), the total scattered wavefields due to perturbation $\delta\lambda$ can be written as the summation of P-P, P-SV and P-SH scattered wavefields:

$$\delta\bar{\mathbf{u}}\left(\mathbf{r},\omega\right) = A\delta\lambda + 0 + 0. \tag{42}$$

where A indicates the amplitude:

$$A = -U\frac{\omega^2 \mathbf{exp}\left(-ik_\alpha r\right)}{4\pi\tilde{\rho}\tilde{\alpha}^4 r}. \tag{43}$$

Because the moment tensor source due to perturbation $\delta\lambda$ is proportional to the divergence of the incident wavefields $\nabla \cdot \grave{\mathbf{u}}$, it only radiates compressional wavefileds and never produce scattered shear wavefields. So, the scattered SV and SH wavefields are all zeros. Furthermore, we can notice that the Fréchet derivative with respect to λ is independent of inclination angle and azimuthal angle:

$$\frac{\partial\bar{\mathbf{u}}\left(\mathbf{r},\omega\right)}{\partial\lambda} = A. \tag{44}$$

While the perturbation $\delta\mu$ causes a much more complex moment tensor source:

$$\frac{\partial M_{ij}^{\mathrm{iso}}}{\partial\mu} = 2\tilde{e}_{ij}. \tag{45}$$

The total scattered wavefields caused by perturbation $\delta\mu$ can be derived following the steps from equation (36) to equation (44). When considering incident plane P wave propagates

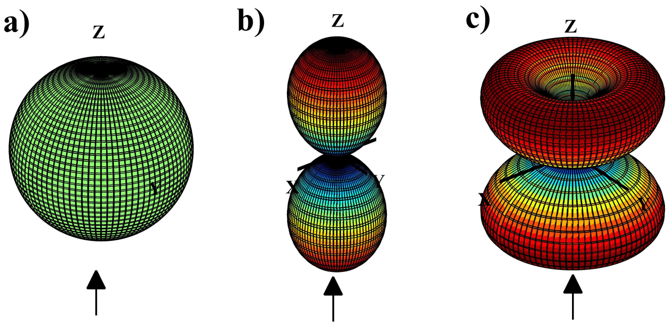

FIG. 2. Scattering patterns by the isotropic and elastic heterogeneity. (a) shows the P-P scattering pattern due to the perturbation $\delta\lambda$. (b) and (c) show the P-P and P-SV scattering patterns due to the perturbation of the shear modulus $\delta\mu$.

along the positive direction of z axis (ϑ=0^o and φ=90^o), the total scattered wavefields can be obtained as:

$$\delta\bar{\mathbf{u}}\left(\mathbf{r},\omega\right) = 2A\cos^2\theta\delta\mu - B\sin 2\theta\delta\mu + 0. \tag{46}$$

where θ indicates the angle between the scattered wavefields and z axis and B is the amplitude of the P-SV scattered wavefields:

$$B = -U\frac{\omega^2\mathbf{exp}\left(-ik_\beta r\right)}{4\pi\tilde{\rho}\tilde{\alpha}\tilde{\beta}^3 r}. \tag{47}$$

The P-SH scattered wavefields is 0. Taking partial derivative with respect to μ gives the Fréchet derivative:

$$\frac{\partial\mathbf{u}\left(\mathbf{r},\omega\right)}{\partial\mu} = 2A\cos^2\theta - B\sin 2\theta. \tag{48}$$

So, the P-P scattering coefficient (or radiation pattern) due to $\delta\lambda$, the P-P and P-SV scattering coefficients due to $\delta\mu$ can be obtained as:

$$\boldsymbol{\mathcal{R}}^{\lambda}_{PP}\left(\theta,\phi\right) = 1, \boldsymbol{\mathcal{R}}^{\mu}_{PP}\left(\theta,\phi\right) = 2\cos^2\theta, \boldsymbol{\mathcal{R}}^{\mu}_{PSV}\left(\theta,\phi\right) = -\sin 2\theta. \tag{49}$$

We can notice that they are independent of azimuthal angle ϕ, which is the opening angle between scattered wavefields and x axis. Figure 2a shows the P-P scattering pattern due to the perturbation $\delta\lambda$ and Figures 2b and c show the P-SV and P-SH scattering patterns due to perturbation $\delta\mu$. The arrows indicate the incident direction of the plane P wave. The detailed analysis for incident SV wave and SH wave can be found in Wu and Aki (1985b,a).

While when parameterizing the isotropic inclusion using elastic constants ($c_{11} = \lambda + 2\mu$, $c_{44} = \mu$ and $(c_{11} - 2c_{44}) = \lambda$), the moment tensor source is expressed as:

$$\delta M^{\mathrm{iso}}_{ij} = \left[\delta c_{11}\left(\nabla\cdot\grave{\mathbf{u}}\right) - 2\delta c_{44}\left(\nabla\cdot\grave{\mathbf{u}} - e_{ii}\right)\right]\delta_{ij} + 2\delta c_{44}e_{ij}. \tag{50}$$

The perturbation δc_{11} causes a explosive-type source, which is consistent with $\delta\lambda$. However, the perturbation δc_{44} causes a double couple source and the scattering coefficients become (ϑ=0^o and φ=90^o):

$$\boldsymbol{\mathcal{R}}_{PP} = -2\sin^2\theta, \boldsymbol{\mathcal{R}}_{PSV} = -\sin 2\theta, \boldsymbol{\mathcal{R}}_{PSH} = -\sin 2\phi\left(\sin\theta + \sin\phi\right). \tag{51}$$

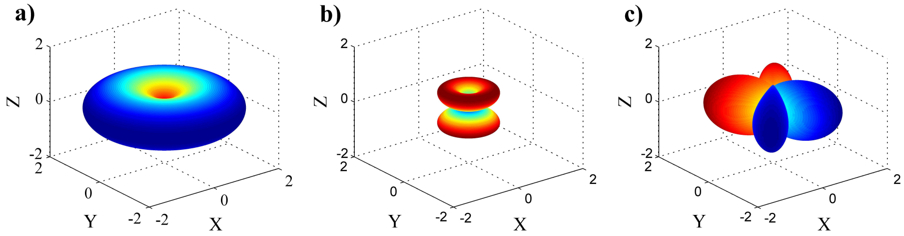

FIG. 3. Scattering patterns when parameterizing isotropic inclusion using elastic constants. (a), (b) and (c) show the P-P, P-SV and P-SH scattering patterns due to the perturbation δc_{44}.

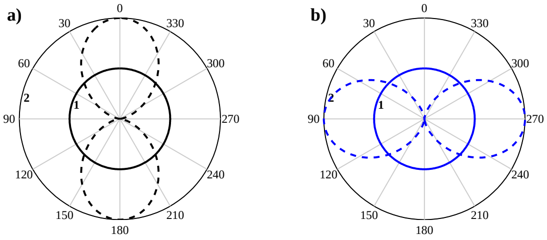

FIG. 4. Scattering patterns in x-z plane for different parameterizations. (a) show the P-P scattering patterns by perturbations $\delta\lambda$ (black-solid line) and $\delta\mu$ (black-dash line). (b) show the P-P scattering patterns by perturbations δc_{11} (blue-solid line) and δc_{44} (blue-dash line).

The P-P, P-SV and P-SH scattering patterns due to δc_{44} are plotted in Figures 3a, b and c respectively. We can notice that the P-SH scattering is associated with azimuth angle ϕ when ϑ=0° and φ=0°.

Here, we can compare the inversion sensitivities when parameterizing the isotropic elastic media using Lamé constants (λ and μ) and elastic stiffness coefficients (c_{11} and c_{44}). The black-solid line and black-dash line in Figure 4a denote the scattering patterns due to $\delta\lambda$ and $\delta\mu$. We can observe that the scattered energy by the perturbations $\delta\lambda$ and $\delta\mu$ are coupled together for precritical reflection survey (0°-30°). In this condition, it will be more chanllenging for us the estimate the properties with reflection FWI. The blue-solid line and blue-dash line in Figure 4b denote the scattering patterns due to δc_{11} and δc_{44}. It can be seen that most of the scattered energy is contributed by δc_{44} for precritical reflection survey. Hence, it will be easier for us to estimate the elastic coefficients directly for the isotropic model.

Inversion Sensitivity of Parallel Vertical Fractures

The FWI sensitivities for anisotropic media has been studied by the many researchers in recent years (Gholami, 2012; Operto et al., 2013; Alkhalifah and Plessix, 2014), for tackling the trade-off or crosstalk issue in multi-parameter FWI. Most of the current studies focus on the 2D VTI media. To estimate the fracture properties using FWI method, the inversion sensitivity analysis is essential to determine the parameters classes and design the acquisition geometry. In this section, we discussed the inversion sensitivities for the simplest parallel vertical fracture model, which is known as transverse isotropy with horizontal symmetry axis (HTI media). The analysis is carried out in 3D with spherical coordinates.

This is because the fracture orientation, indicated by the azimuthal angle ϕ, is extremely important for fractured reservoir characterization.

Generally, the HTI model is caused by a system of parallel vertical circular ("penny-shaped") cracks embedded in an isotropic background (Bakulin et al., 2000; Tsvankin, 2001). And it has two mutually orthogonal vertical planes of symmetry, the symmetry axis plane and the isotropy plane, as shown in Figure 1.6 of (Tsvankin, 2001). The HTI model is a degenerated case of an orthorhombic symmetry with only 5 independent elastic stiffness coefficients, which are c_{11}, c_{33}, c_{44}, c_{55} and c_{13}. We can follow the steps in the above section to calculate the scattering patterns and Fréchet derivative for the vertically fractured media. According to equation (33), the scattered wavefields with plane P-wave incidence can be reformulated as:

$$\delta \mathbf{u}^{\mathrm{P}}\left(\mathbf{r}, \omega\right) = -\frac{\omega^2 \mathbf{exp}(-ik_\xi r)}{4\pi\rho\alpha\xi^3 r}\left[\mathbf{D}^{\dagger}\delta\bar{\mathbf{M}}^{\mathrm{HTI}}\mathbf{R}\right], \tag{52}$$

where ξ indicates P-wave velocity α or S-wave velocity β and k_ξ denotes the corresponding wavenumber. The matrix $\mathbf{D}$ can be $\mathbf{R}$, $\mathbf{\Theta}$ and $\mathbf{\Phi}$ for P-P, P-SV and P-SH scattered wavefields respectively. $\delta\bar{\mathbf{M}}$ is the reduced moment tensor source. And we define $\mathbf{D}^{\dagger}\delta\bar{\mathbf{M}}^{\mathrm{HTI}}\mathbf{R}$ as the scattering coefficients.

According to the stiffness coefficients matrix for HTI media, the corresponding perturbation matrix $\delta\mathbf{c}^{\mathrm{HTI}}$ can be expressed as:

$$\delta\mathbf{c}^{\mathrm{HTI}} = \begin{bmatrix} \delta c_{11} & \delta c_{13} & \delta c_{13} & 0 & 0 & 0 \\ \delta c_{13} & \delta c_{33} & \delta\nu & 0 & 0 & 0 \\ \delta c_{13} & \delta\nu & \delta c_{33} & 0 & 0 & 0 \\ 0 & 0 & 0 & \delta c_{44} & 0 & 0 \\ 0 & 0 & 0 & 0 & \delta c_{55} & 0 \\ 0 & 0 & 0 & 0 & 0 & \delta c_{55} \end{bmatrix}. \tag{53}$$

where $\delta\nu = \delta c_{33} - 2\delta c_{44}$. Similarly, the moment tensor source caused by the perturbations of the elastic constants can be obtained as:

$$\delta\mathbf{M}^{\mathrm{HTI}} = \begin{bmatrix} \delta c_{11}e_{11} + \delta c_{13}e_{22} + \delta c_{13}e_{33} & 2\delta c_{55}e_{12} & 2\delta c_{55}e_{13} \\ 2\delta c_{55}e_{12} & \delta c_{13}e_{11} + \delta c_{33}e_{22} + \delta\nu e_{33} & 2\delta c_{44}e_{23} \\ 2\delta c_{55}e_{13} & 2\delta c_{44}e_{23} & \delta c_{13}e_{11} + \delta\nu e_{22} + \delta c_{33}e_{33} \end{bmatrix}.$$

Considering the incident plane P-wave $\dot{\mathbf{u}}(\mathbf{r})$ with incident angle ϑ and azimuthal angle φ (as shown in equation (37)), the explicit expressions of the strain components are listed in Appendix A. If the symmetry axis plane of HTI obstacle is parallel to the x-z plane, azimuthal angle ϕ of the scattered wavefields can be used to indicate the source-receiver azimuth. Firstly, we can examine the scattered wavefields caused by the elastic constant perturbation δc_{33} for HTI model. When keeping the perturbations δc_{11}, δc_{13}, δc_{55}, and δc_{44} as zero, the perturbation δc_{33} contributes to the equivalent moment source:

$$\delta \mathbf{M}^{\mathrm{HTI}} = \delta c_{33} \begin{bmatrix} 0 & 0 & 0 \\ 0 & e_{22} + e_{33} & 0 \\ 0 & 0 & e_{22} + e_{33} \end{bmatrix}, \tag{54}$$

Taking out the wavenumber and $\mathbf{exp}\,(i\psi)$ parts and normalizing the perturbation $\delta c_{33} = 1$, the reduced moment tensor source $\delta \bar{\mathbf{M}}$ can be defined as:

$$\delta \bar{\mathbf{M}} = \begin{bmatrix} 0 & 0 & 0 \\ 0 & (\sin \vartheta^2 \sin \varphi^2 + \cos \vartheta^2) & 0 \\ 0 & 0 & (\sin \vartheta^2 \sin \varphi^2 + \cos \vartheta^2) \end{bmatrix}. \tag{55}$$

Substituting the reduced moment tensor source into equation (33) yields the P-P, P-SV and P-SH scattered wavefields and Fréchet derivative. The P-P, P-SV and P-SH scattering coefficients (or radiation patterns) describe the amplitude variations of the Fréchet derivative with respect to elastic constant c_{33}. They can be used to analyze the wavefields responses with varying scattering angle θ and azimuthal angle ϕ, as shown in the following.

$$\begin{aligned} \boldsymbol{\mathcal{R}}_{PP} &= \mathbf{R}^{\dagger} \delta \bar{\mathbf{M}}^{\mathrm{HTI}} \mathbf{R} \\ &= \left(\sin^2 \theta \sin^2 \phi + \cos^2 \theta\right) \left(\sin \vartheta^2 \sin \varphi^2 + \cos \vartheta^2\right), \\ \boldsymbol{\mathcal{R}}_{PSV} &= \boldsymbol{\Theta}^{\dagger} \delta \bar{\mathbf{M}}^{\mathrm{HTI}} \mathbf{R} \\ &= -\frac{1}{2} \sin 2\theta \cos^2 \phi \left(\sin \vartheta^2 \sin \varphi^2 + \cos \vartheta^2\right), \\ \boldsymbol{\mathcal{R}}_{PSH} &= \boldsymbol{\Phi}^{\dagger} \delta \bar{\mathbf{M}}^{\mathrm{HTI}} \mathbf{R} \\ &= \frac{1}{2} \sin \theta \sin 2\phi \left(\sin \vartheta^2 \sin \varphi^2 + \cos \vartheta^2\right). \end{aligned} \tag{56}$$

To examine the amplitude variations of the wavefields responses with varying the scattering angle and azimuthal angle, we design two acquisition geometries as shown in Figure 8. We assume that the symmetry axis of the HTI obstacle is consistent with the x axis and thus its isotropic plane lies in the y-z plane. And the azimuthal angle of the scattered wavefields can be used to indicate the source-receiver azimuth. In the first acquisition geometry, as shown in Figure 8a, we defines 4 source-receiver lines with azimuthal angle ϕ=0°,30°,60° and 90°. And then we vary the opening angle between the incident wavefields and scattered wavefields from 0° to 360°. In this condition, we can examine the wavefields responses due to the parameter perturbation δc_{33} with varying the scattering angle at different azimuthal angles.

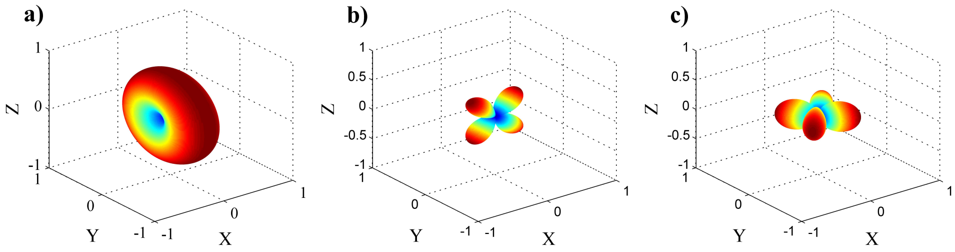

FIG. 5. Scattering patterns due to the perturbation of δc_{33} when $\vartheta = 30^o$ and $\varphi = 0^o$. (a), (b) and (c) show the P-P, P-SV and P-SH scattering patterns respectively.

The scattering patterns due to δc_{33} with varying scattering angle at fixed azimuthal angles 0^o, 30^o, 60^o and 90^o are illustrated in Figures 9a, b, c and d respectively.

The second acquisition geometry is presented in Figure 8. We vary the source-receiver azimuth from 0^o to 360^o and fix the opening angle at 0^o, 60^o, 120^o and 180^o respectively. The corresponding incident angle and scattering angle pair (ϑ, θ) are (180^o, 0^o), (150^o, 30^o), (120^o, 60^o) and (90^o, 90^o).

The scattering patterns due to other elastic constants perturbations can also be calculated following the above steps. And the total scattered wavefields by the HTI obstacle are the superpositions of the scattered wavefields due to all of the parameters' perturbations. The Fréchet derivative and scattering patterns for incident SV-wave and SH-wave are illustrated in Appendix A. Figure 11 shows the scattering patterns by the perturbations of the elastic constants δc_{11}, δc_{33}, δc_{13} and δc_{55} for HTI model with incident P-wave(ϑ=30^o and φ=0^o). The scattering coefficients by δc_{44} are all zeros. We can observe that in y-z plane, the isotropic plane of the HTI obstacle, the scattered energy mainly comes from P-P and P-SH scattering. In x-z plane, the symmetry axis plane of the HTI obstacle, the scattered energy mainly comes from P-P and P-SV scattering. While in x-y plane, the azimuth plane, the scattered energy mainly comes from P-P and P-SH scattering.

INVERSION SENSITIVITY OF ORTHORHOMBIC FRACTURES

The majority of the existing studies for fracture properties estimation mainly focus on VTI and HTI anisotropy, the simplest effective models for describing the fractured reservoirs. While both HTI and VTI media with single fracture system are actually special cases of an orthorhombic symmetry, which is also commonly existed in naturally fractured reservoirs(Wild and Crampin, 1991; Schoenberg and Helbig, 1997; Tsvankin, 1997a). The difficulties in dealing with the 9 independent elastic constants in orthorhombic fracture preclude this model from application in exploration geophysics. In this section, the seismic scattering due to a local orthorhombic fracture obstacle is discussed and we provide the explicit expressions of the 3D Fréchet derivative with respect to the 9 elastic stiffness coefficients in orthorhombic media. Furthermore, the sensitivity kernels and scattering patterns for these elastic constants are analyzed.

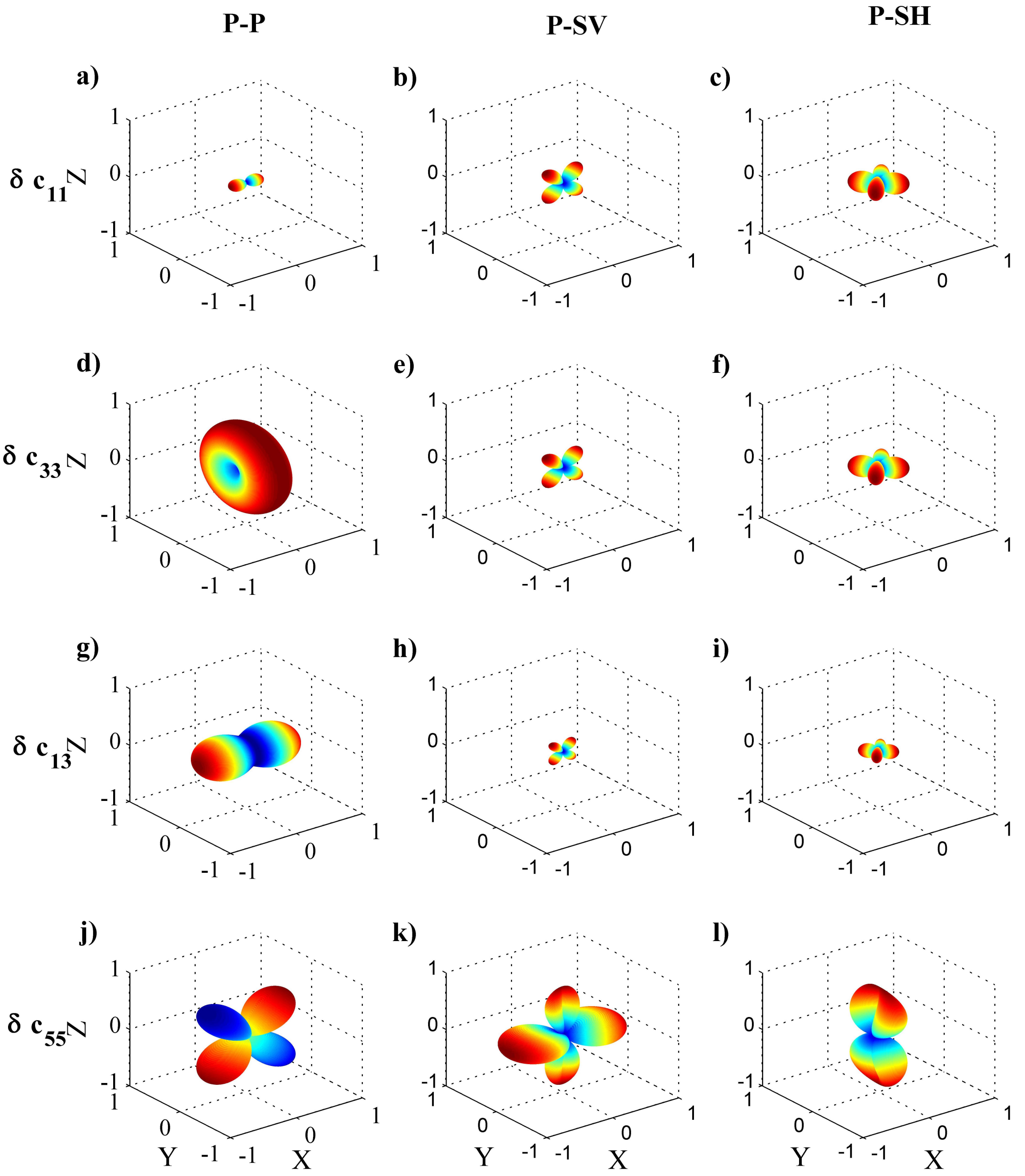

FIG. 6. Scattering patterns due to the perturbation of δc_{11}, δc_{33}, δc_{13} and δc_{55} when $\vartheta = 30^{\circ}$ and $\varphi = 0^{\circ}$. The first, second and third column show the P-P, P-SV and P-SH scattering patterns respectively.

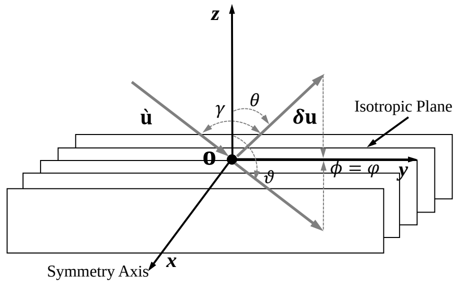

FIG. 7. The scattering configuration. The symmetry axis of the HTI obstacle is consistent with axis x and the isotropic plane lies in y-z plane. $\grave{\mathbf{u}}$ and $\delta\mathbf{u}$ in (a) are the incident wave and scattered wave in y-z plane. ϑ and φ are the incident angle and azimuth angle of the incident wave. θ and ϕ are scattering angle and azimuth angle of the scattered wave. γ is the opening angle between the incident wave and scattered wave.

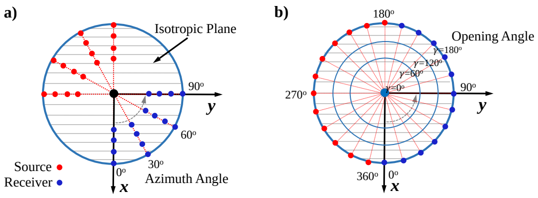

FIG. 8. The acquisition geometries. In (a), the sources and receivers are distributed along 4 azimuth lines (0°, 30°, 60° and 90°) when the opening angle γ ranges from 0° to 360°. In (b), the single source-receiver pairs are located at 4 opening angle circles (0°, 60°, 120° and 180°) with varying the azimuth angle from from 0° to 360°. The red and blues points indicate the sources and receivers.

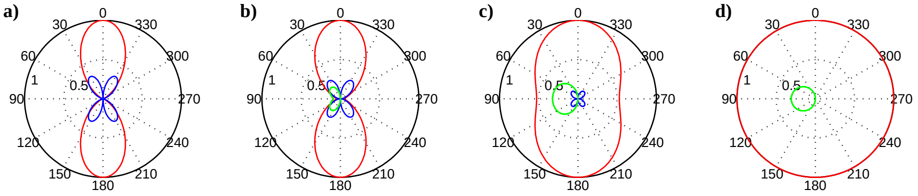

FIG. 9. Scattering patterns due to the perturbation of δc_{33}. (a), (b), (c) and (d) show the scattering patterns when the opening angle between the incident wavefields and scattered wavefields is fixed at 0°, 60°, 120° and 180° with varying the azimuthal angle ϕ from 0° to 360°. The corresponding angle pair (ϑ,θ) is $((0^{\circ},0^{\circ}))$, $(150^{\circ},30^{\circ})$, $(120^{\circ},60^{\circ})$ and $(90^{\circ},90^{\circ})$. The black-dash curves, black-sold curves and grey-solid curves indicate the P-P, P-SV and P-SH scattering respectively. Note: The P-SV scattering coefficients in (d) are enlarged by 20 times to be observed.

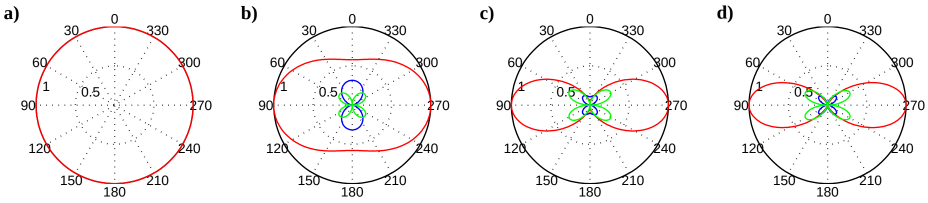

FIG. 10. Scattering patterns due to the perturbation of δc_{33}. (a), (b), (c) and (d) show the scattering patterns when the opening angle between the incident wavefields and scattered wavefields is fixed at 0^o, 60^o, 120^o and 180^o with varying the azimuthal angle ϕ from 0^o to 360^o. The corresponding angle pair (ϑ, θ) is $(0^o, 0^o)$, $(150^o, 30^o)$, $(120^o, 60^o)$ and $(90^o, 90^o)$. The black-dash curves, black-sold curves and grey-solid curves indicate the P-P, P-SV and P-SH scattering respectively. Note: The P-SV scattering coefficients in (d) are enlarged by 20 times to be observed.

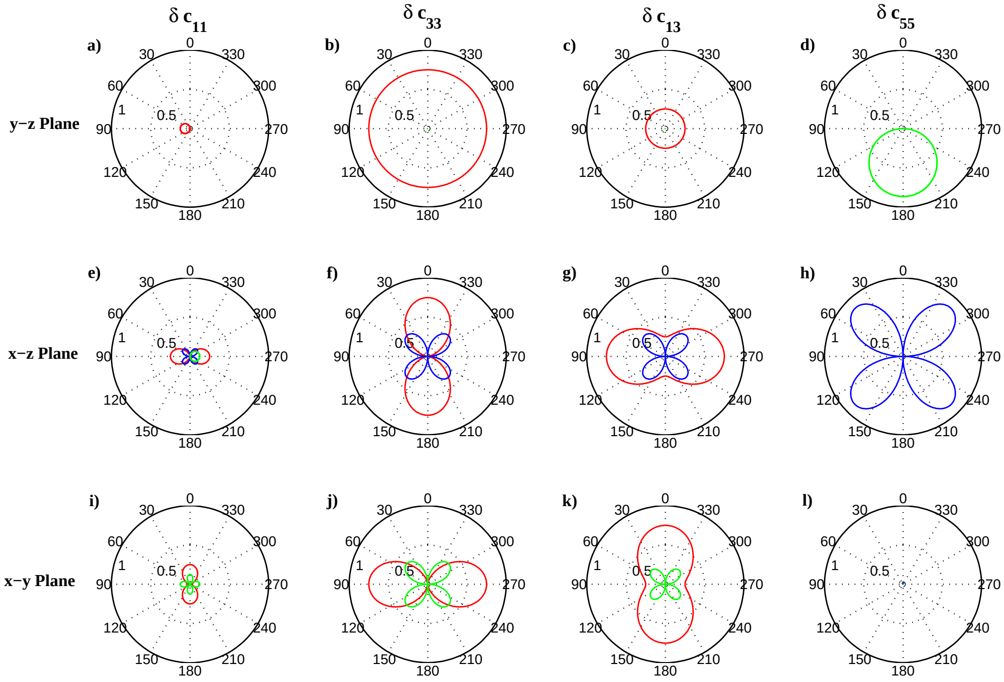

FIG. 11. Scattering patterns due to the perturbations of δc_{11}, δc_{33}, δc_{13} and δc_{55}. The first row, second row and third row show the scattering patterns in y-z plane, x-z plane and x-y plane respectively. The red, blue and green lines indicate the P-P, P-SV and P-SH scattering patterns respectively.

$$\delta\mathbf{c}^{\mathrm{ort}} = \begin{bmatrix} \delta c_{11} & \delta c_{12} & \delta c_{13} & 0 & 0 & 0 \\ \delta c_{12} & \delta c_{22} & \delta c_{23} & 0 & 0 & 0 \\ \delta c_{13} & \delta c_{23} & \delta c_{33} & 0 & 0 & 0 \\ 0 & 0 & 0 & \delta c_{44} & 0 & 0 \\ 0 & 0 & 0 & 0 & \delta c_{55} & 0 \\ 0 & 0 & 0 & 0 & 0 & \delta c_{66} \end{bmatrix}. \tag{57}$$

$$\delta\mathbf{M}^{\mathrm{Ort}} = \begin{bmatrix} \delta c_{11}e_{11} + \delta c_{12}e_{22} + \delta c_{13}e_{33} & 2\delta c_{66}e_{12} & 2\delta c_{55}e_{13} \\ 2\delta c_{66}e_{12} & \delta c_{12}e_{11} + \delta c_{22}e_{22} + \delta c_{23}e_{33} & 2\delta c_{44}e_{13} \\ 2\delta c_{55}e_{13} & 2\delta c_{44}e_{13} & \delta c_{13}e_{11} + \delta c_{23}e_{22} + \delta c_{33}e_{33} \end{bmatrix}. \tag{58}$$

An example of perturbation leading to two dipoles source radiation pattern is δc_{13}. In this case, the moment tensor is:

$$\delta\mathbf{M} = \begin{bmatrix} \delta c_{13}e_{33}^{0} & 0 & 0 \\ 0 & 0 & 0 \\ 0 & 0 & \delta c_{13}e_{11}^{0} \end{bmatrix}. \tag{59}$$

Figures 12 and 13 show the 3D scattering patterns due to the perturbations of δc_{11}, δc_{22}, δc_{33}, δc_{44}, δc_{55}, δc_{66}, δc_{23}, δc_{13} and δc_{12} in orthorhombic media. Figures 14 and 15 show the scattering patterns of the these elastic constants in x-z, y-z and x-y plane respectively.

APPENDIX A: 3D FRÉCHET DERIVATIVE AND SCATTERING PATTERNS FOR PLANE SV-WAVE AND SH-WAVE INCIDENCE

Consider the incident plane SV-wave with incident angle ϑ and azimuth angle φ:

$$\dot{\mathbf{u}}^{\mathrm{SV}}(\mathbf{r}) = \mathbf{U}^{\mathrm{SV}}\mathbf{exp}\left[i(\omega t - k_\beta \mathbf{U}\cdot\mathbf{n})\right], \tag{60}$$

where $\mathbf{U}^{\mathrm{SV}} = (\cos\vartheta\cos\varphi\mathbf{x} + \cos\vartheta\sin\varphi\mathbf{y} - \sin\vartheta\mathbf{z})$. And the strain components of the incident SV-wave are:

$$e_{ij} = -\tfrac{1}{2}ik_\beta\left(U_i^{\mathrm{SV}}U_j + U_j^{\mathrm{SV}}U_i\right)\mathbf{exp}\left[i(\omega t - k_\beta\mathbf{U}\cdot\mathbf{n})\right]. \tag{61}$$

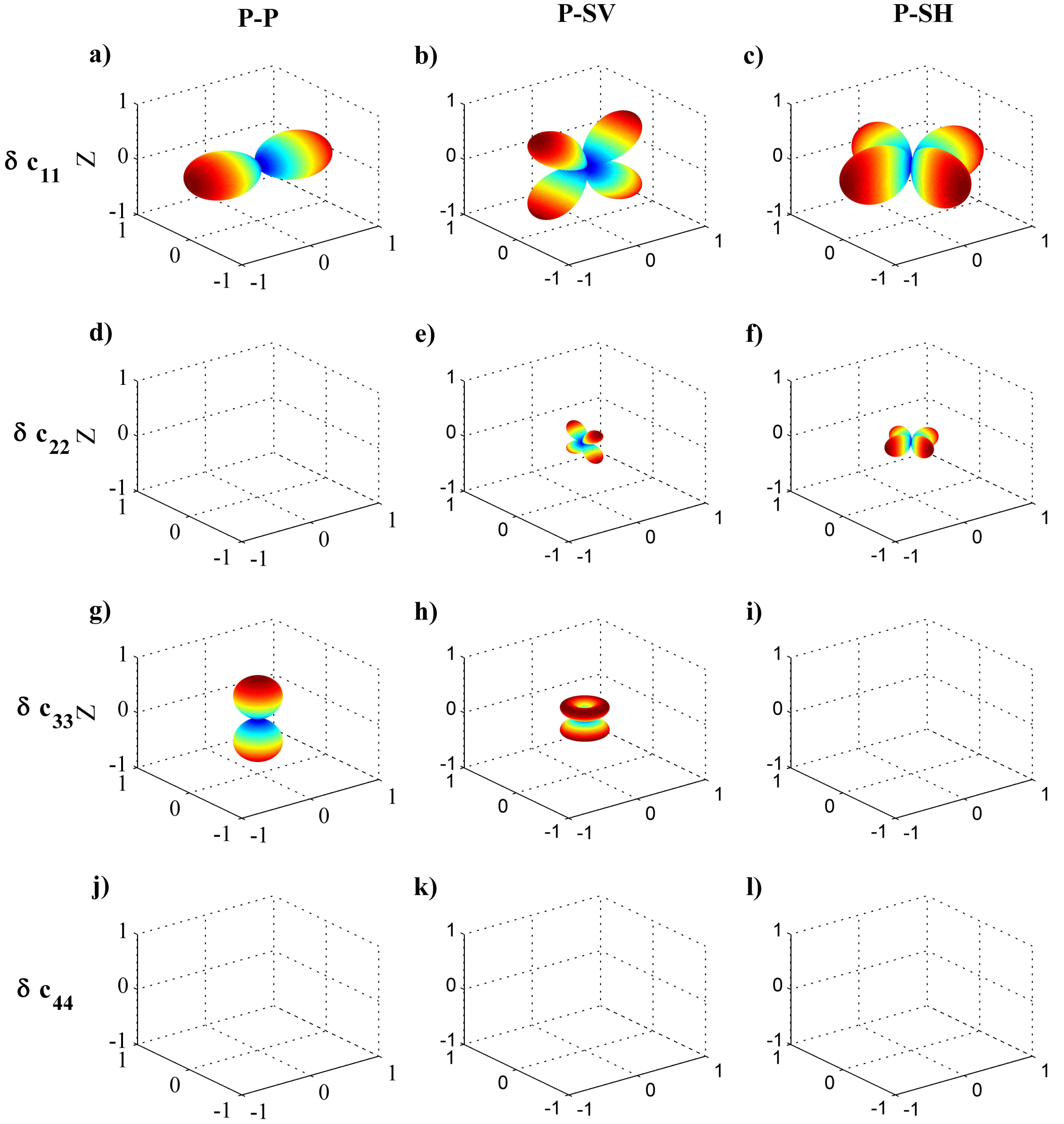

FIG. 12. P-P, P-SV and P-SH scattering patterns due to the perturbation of δc_{11}, δc_{22}, δc_{33} and δc_{44} in orthorhombic media.

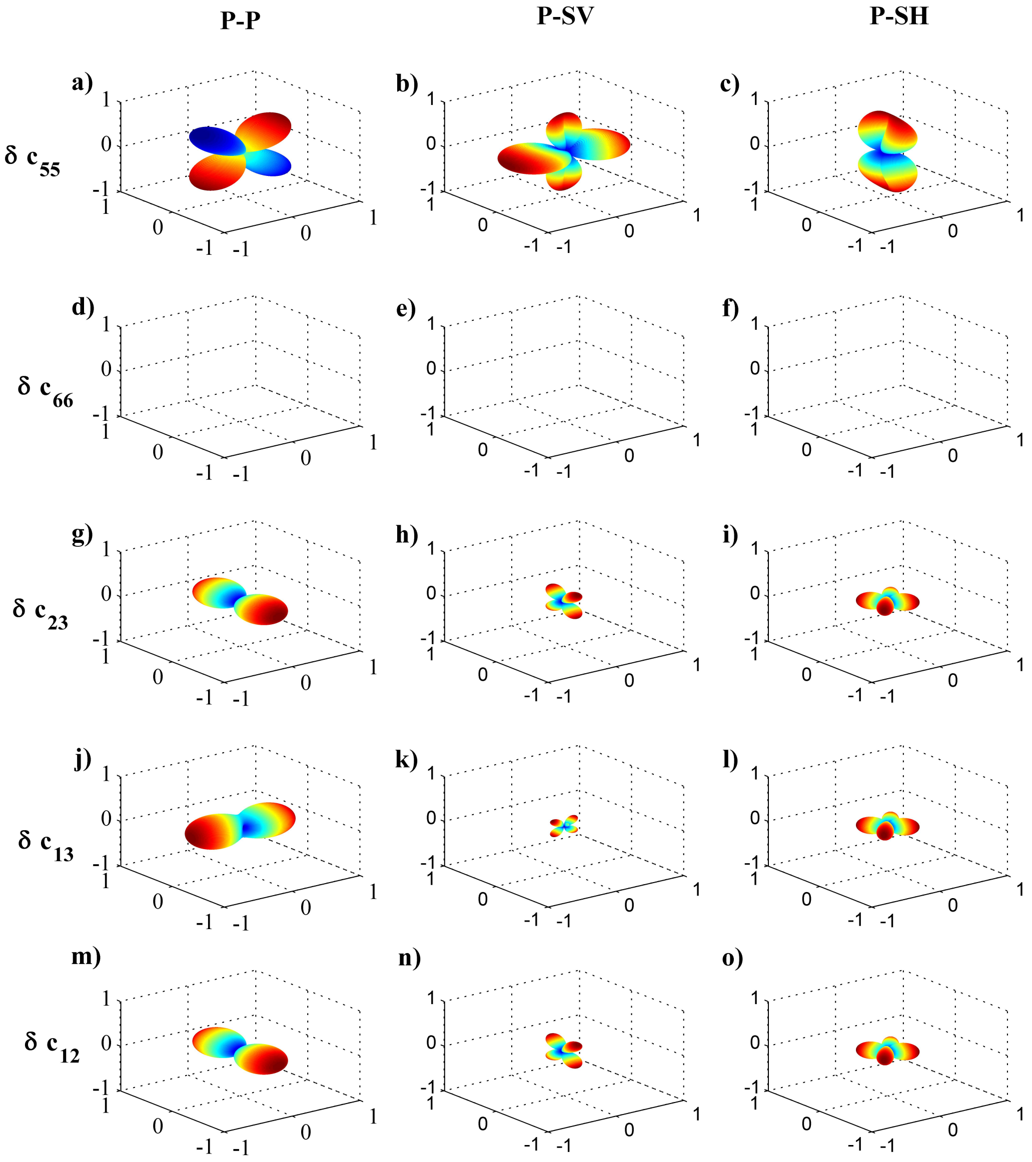

FIG. 13. P-P, P-SV and P-SH Scattering patterns due to the perturbation of δc_{55}, δc_{66}, δc_{23}, δc_{13} and δc_{12} in orthorhombic media.

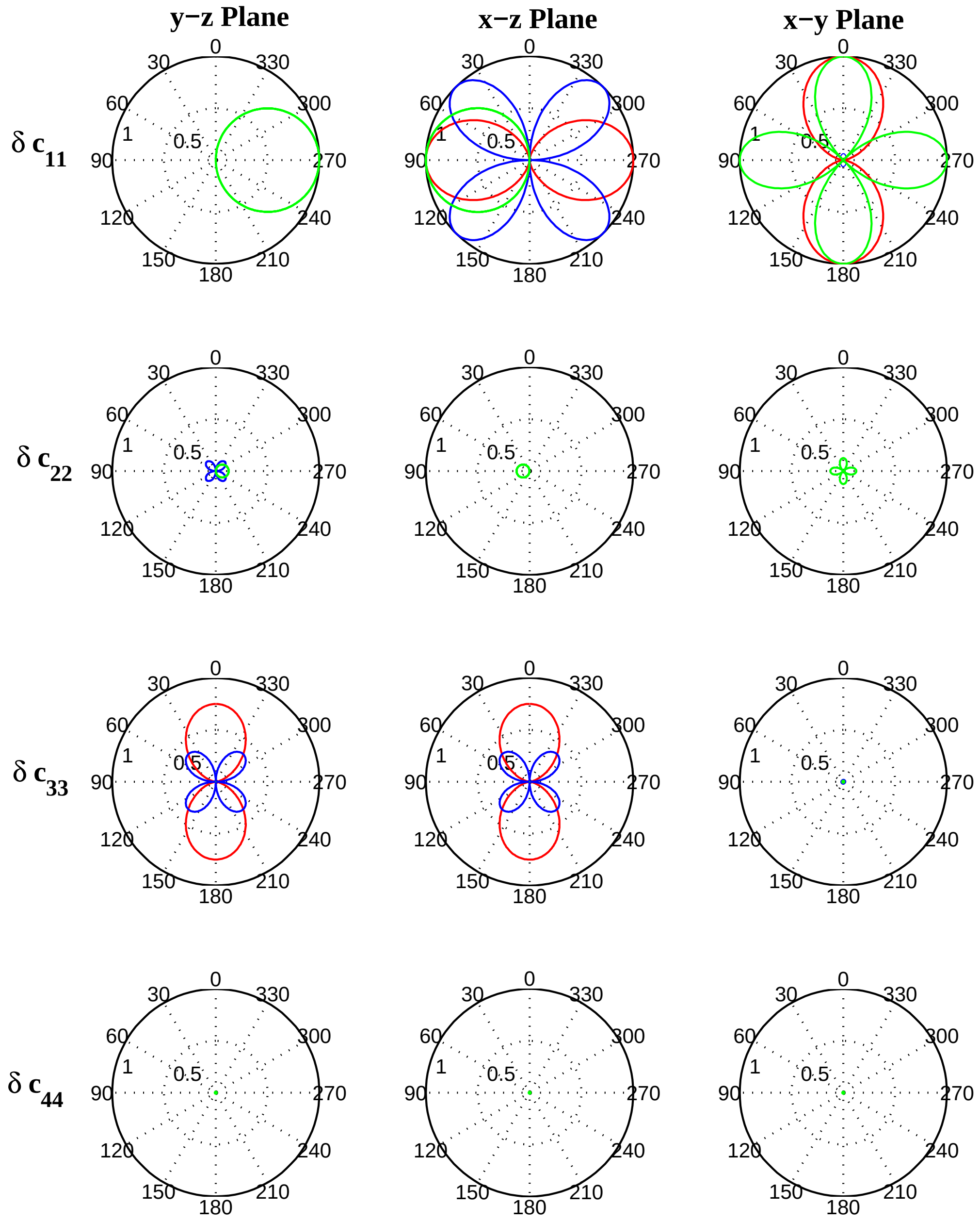

FIG. 14. P-P, P-SV and P-SH Scattering patterns due to the perturbation of δc_{11}, δc_{22}, δc_{33} and δc_{44} in y-z, x-z and x-y planes respectively.

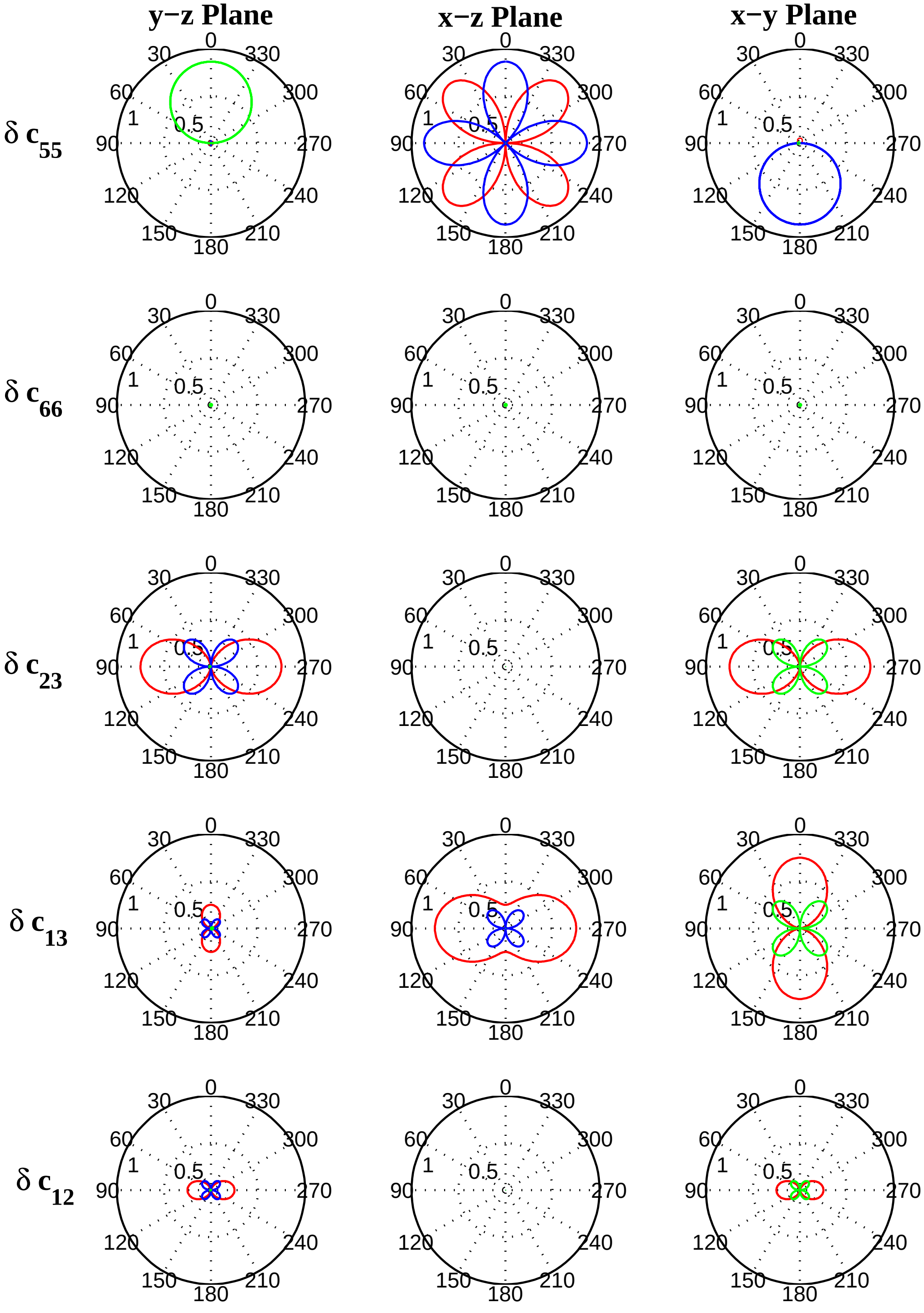

FIG. 15. P-P, P-SV and P-SH Scattering patterns due to the perturbation of δc_{55}, δc_{66}, δc_{23}, δc_{13} and δc_{12} in y-z, x-z and x-y planes respectively.

Thus, we can construct the moment tensor source $\delta\mathbf{M}$ caused by the elastic constants perturbations. The scattered wavefields with plane SV-wave incidence can be reformulated as:

$$\delta\mathbf{u}^{\text{SV}}(\mathbf{r},\omega) = -\frac{\omega^2\mathbf{exp}(-ik_\xi r)}{4\pi\rho\beta\xi^3 r}\left(\mathbf{D}^\dagger\delta\bar{\mathbf{M}}\mathbf{R}\right), \tag{62}$$

where ξ indicates P-wave velocity α or S-wave velocity β and k_ξ denotes the corresponding wavenumber. $\delta\bar{\mathbf{M}}$ is the reduced moment tensor source when removing $-ik_\beta$ and $\mathbf{exp}\left[i\left(\omega t - k_\beta\mathbf{U}\cdot\mathbf{n}\right)\right]$. Taking partial derivative with respect to model parameter m, where $m \in (c_{11}, c_{33}, c_{44}, c_{55}, c_{13})$ for HTI model and $m \in (c_{11}, c_{22}, c_{33}, c_{44}, c_{55}, c_{66}, c_{23}, c_{13}, c_{12})$ for orthorhombic model (the perturbation of density is ignored), yields the 3D Fréchet derivative for SV-wave incidence:

$$\frac{\partial\mathbf{u}^{\text{SV}}(\mathbf{r},\omega)}{\partial m} = -\frac{\omega^2\mathbf{exp}(-ik_\xi r)}{4\pi\rho\beta\xi^3 r}\left(\mathbf{D}^\dagger\frac{\partial\bar{\mathbf{M}}}{\partial m}\mathbf{R}\right), \tag{63}$$

$\mathbf{D}^\dagger\delta\bar{\mathbf{M}}\mathbf{R}$ is defined as the scattering coefficient (or scattering pattern). The vector $\mathbf{D}$ can be $\mathbf{R}$, $\boldsymbol{\Theta}$ and $\boldsymbol{\Phi}$ for SV-P, SV-SV and SV-SH scattered wavefields and they can be written in matrix form:

$$\mathbf{R} = \begin{bmatrix} \sin\theta\cos\phi \\ \sin\theta\sin\phi \\ \cos\theta \end{bmatrix}, \boldsymbol{\Theta} = \begin{bmatrix} \cos\theta\cos\phi \\ \cos\theta\sin\phi \\ -\sin\theta \end{bmatrix}, \boldsymbol{\Phi} = \begin{bmatrix} -\sin\phi \\ \cos\phi \\ 0 \end{bmatrix}. \tag{64}$$

Here, we take the scattered SV-P, SV-SV and SV-SH wavefields for the HTI model for illustration. The elements of reduced meoment tensor source $\delta\bar{\mathbf{M}}^{\text{HTI}}$ can be written as:

$$\begin{bmatrix} \delta\bar{M}_{11}^{\text{HTI}} \\ \delta\bar{M}_{22}^{\text{HTI}} \\ \delta\bar{M}_{33}^{\text{HTI}} \\ \delta\bar{M}_{23}^{\text{HTI}} \\ \delta\bar{M}_{13}^{\text{HTI}} \\ \delta\bar{M}_{12}^{\text{HTI}} \end{bmatrix} = \begin{bmatrix} \delta c_{11}U_1^{\text{SV}}U_1 + \delta c_{13}U_2^{\text{SV}}U_2 + \delta c_{13}U_3^{\text{SV}}U_3 \\ \delta c_{13}U_1^{\text{SV}}U_1 + \delta c_{33}U_2^{\text{SV}}U_2 + \delta\nu U_3^{\text{SV}}U_3 \\ \delta c_{13}U_1^{\text{SV}}U_1 + \delta\nu U_2^{\text{SV}}U_2 + \delta c_{33}U_3^{\text{SV}}U_3 \\ \delta c_{44}\left(U_2^{\text{SV}}U_3 + U_3^{\text{SV}}U_2\right) \\ \delta c_{55}\left(U_1^{\text{SV}}U_3 + U_3^{\text{SV}}U_1\right) \\ \delta c_{55}\left(U_1^{\text{SV}}U_2 + U_2^{\text{SV}}U_1\right) \end{bmatrix}. \tag{65}$$

The scattered SV-P, SV-SV and SV-SH wavefields can be obtained as:

$$\delta\mathbf{u}(\mathbf{r},\omega)^{\text{SVP}} = A'\mathbf{R}^\dagger\delta\bar{\mathbf{M}}\mathbf{R}, \tag{66}$$

$$\delta\mathbf{u}(\mathbf{r},\omega)^{\text{SVSV}} = B'\boldsymbol{\Theta}^\dagger\delta\bar{\mathbf{M}}\mathbf{R}, \tag{67}$$

$$\delta\mathbf{u}(\mathbf{r},\omega)^{\text{SVSH}} = B'\boldsymbol{\Phi}^\dagger\delta\bar{\mathbf{M}}\mathbf{R}, \tag{68}$$

where A' and B' are:

$$A' = -\frac{\omega^2 \mathbf{exp}(-ik_\alpha r)}{4\pi\rho\beta\alpha^3 r}, B' = -\frac{\omega^2 \mathbf{exp}(-ik_\beta r)}{4\pi\rho\beta^4 r}.$$

For illustration, considering when ϑ=φ=0$^{\mathrm{o}}$, $\mathbf{U}^{\mathrm{SV}}$ and $\mathbf{U}$ becomes:

$$\mathbf{U}^{\mathrm{SV}} = \begin{bmatrix} 1 \\ 0 \\ 0 \end{bmatrix}, \mathbf{U} = \begin{bmatrix} 0 \\ 0 \\ 1 \end{bmatrix} \tag{69}$$

And the reduced moment tensor source becomes:

$$\delta\bar{\mathbf{M}}^{\mathrm{HTI}} = \begin{bmatrix} 0 & 0 & \delta c_{55}\left(U_1^{\mathrm{SV}}U_3 + U_3^{\mathrm{SV}}U_1\right) \\ 0 & 0 & 0 \\ \delta c_{55}\left(U_1^{\mathrm{SV}}U_3 + U_3^{\mathrm{SV}}U_1\right) & 0 & 0 \end{bmatrix}. \tag{70}$$

Substituting it into the equations (66), (67) and (68) yields the scatered SV-P, SV-SV and SV-SH wavefields:

$$\begin{aligned} \delta\mathbf{u}\left(\mathbf{r},\omega\right)^{\mathrm{SVP}} &= \delta c_{55} A' \left(2R_3R_1\right) \\ &= \delta c_{55} A' \sin 2\theta \cos\phi, \\ \delta\mathbf{u}\left(\mathbf{r},\omega\right)^{\mathrm{SVP}} &= \delta c_{55} B' \left(\Theta_3 R_1 + \Theta_1 R_3\right) \\ &= \delta c_{55} B' \left(\cos\theta^2 \cos\phi - \cos\phi \sin\theta^2\right), \\ \delta\mathbf{u}\left(\mathbf{r},\omega\right)^{\mathrm{SVSH}} &= \delta c_{55} B' \left(\Phi_3 R_1 + \Phi_1 R_3\right) \\ &= -\delta c_{55} B' \sin\phi \cos\theta. \end{aligned} \tag{71}$$

The scattering patterns with SV incidence are shown in Figure 16.

Similarly, if we consider the incident plane SH-wave:

$$\grave{\mathbf{u}}^{\mathrm{SH}}(\mathbf{r}) = \mathbf{U}^{\mathrm{SH}} \mathbf{exp}\left[i(\omega t - k_\beta \mathbf{U}\cdot\mathbf{n})\right], \tag{72}$$

where $\mathbf{U}^{\mathrm{SH}} = (-\sin\varphi\mathbf{x} + \cos\varphi\mathbf{y})$. Its strain components can be writtern as:

$$e_{ij} = -\tfrac{1}{2} i k_\beta \left(U_i^{\mathrm{SH}} U_j + U_j^{\mathrm{SH}} U_i\right) \mathbf{exp}\left[i(\omega t - k_\beta \mathbf{U}\cdot\mathbf{n})\right]. \tag{73}$$

And the the 3D Fréchet derivative can be obtained as:

$$\frac{\partial\mathbf{u}^{\mathrm{SH}}\left(\mathbf{r},\omega\right)}{\partial m} = -\frac{\omega^2 \mathbf{exp}(-ik_\xi r)}{4\pi\rho\beta\xi^3 r}\left(\mathbf{D}^\dagger \frac{\partial\bar{\mathbf{M}}}{\partial m}\mathbf{R}\right). \tag{74}$$

And when $\mathbf{D}$ is $\mathbf{R}$, $\boldsymbol{\Theta}$ and $\boldsymbol{\Phi}$, equation (74) denotes the Fréchet derivative with respect to m for SH-P, SH-SV and SH-SH scattered wavefields, as shown in Figure 17.

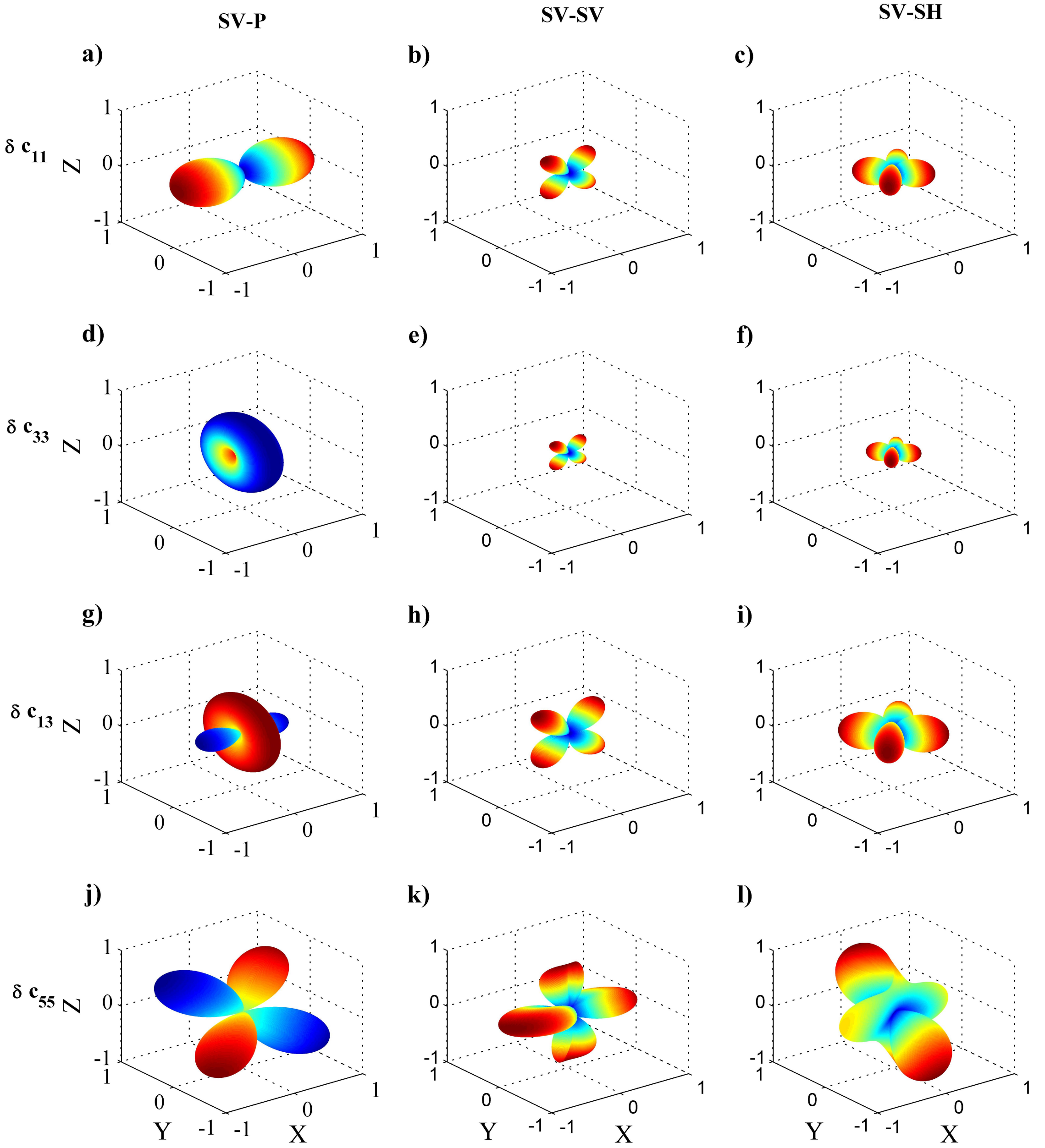

FIG. 16. Scattering patterns with incident SV-wave due to the perturbation of $\delta c_{11}, \delta c_{33}, \delta c_{13}$, and δc_{55} when $\vartheta = 30^{o}$ and $\varphi = 30^{o}$. (a), (b) and (c) show the SV-P, SV-SV and SV-SH scattering patterns respectively.

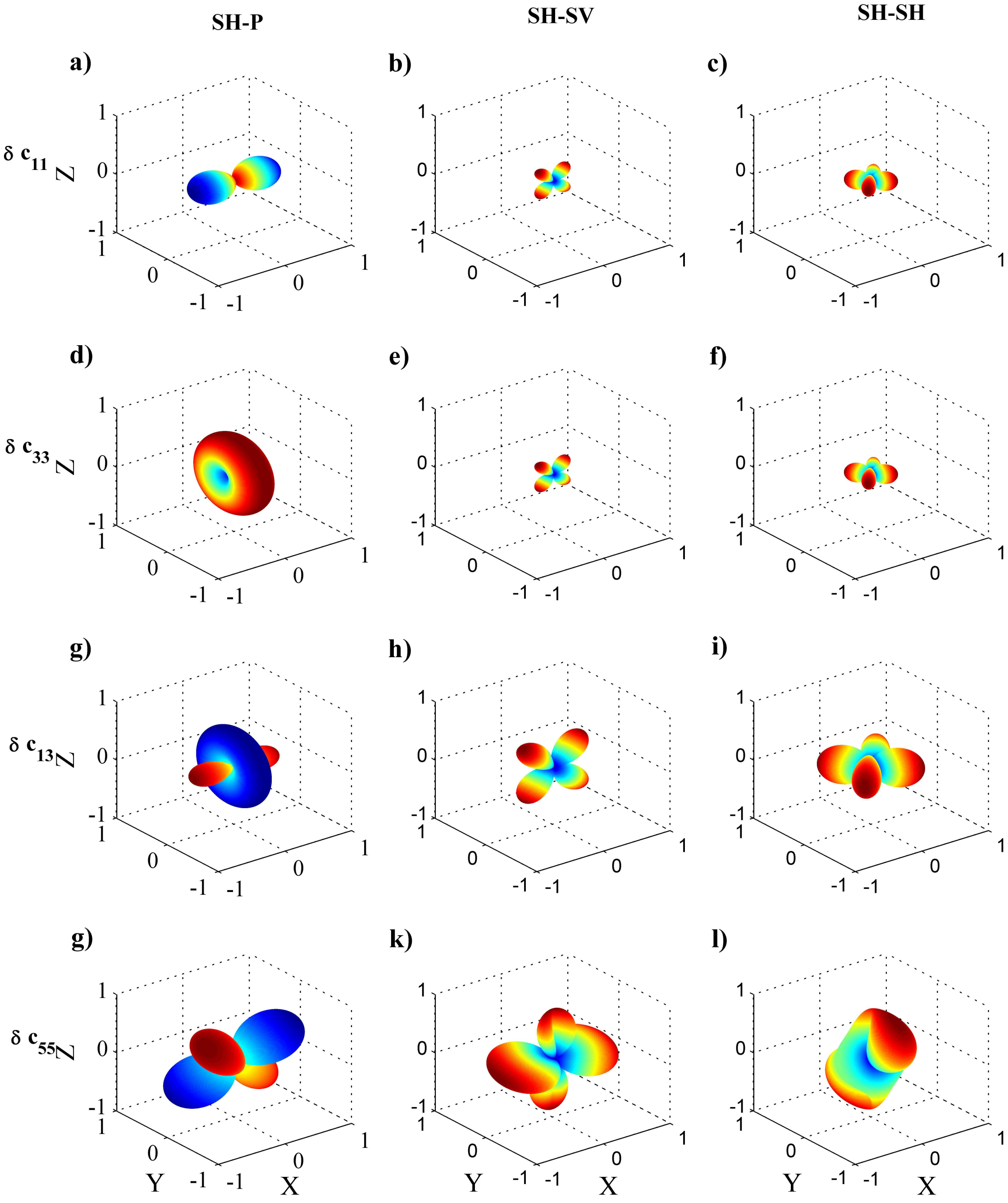

FIG. 17. Scattering patterns with incident SH-wave due to the perturbation of $\delta c_{11}, \delta c_{33}, \delta c_{13} and \delta c_{55}$ when $\vartheta = 30^o$ and $\varphi = 30^o$. (a), (b) and (c) show the SH-P, SH-SV and SH-SH scattering patterns respectively.

]

ACKNOWLEDGEMENTS

We thank the sponsors of CREWES for their support. We also gratefully acknowledge support from NSERC (Natural Science and Engineering Research Council of Canada) through the grant CRDPJ $379744 - 08$. The author greatly appreciates the help from the professors and researchers in ERL (Earth Resources Laboratory) of MIT. Thanks also to Sam Ahmad Zamanian (Shell), Di Yang (Exxon Mobil), Xuan Feng (Jilin University), Hua Wang (MIT) and Sudhish Bakku (MIT) for their valuable discussions.

REFERENCES

Aki, K., and Richards, P. G., 2002, Quantitative Seismology: University Science Books, 2nd edn.

Alkhalifah, T., and Plessix, R., 2014, A recipe for practical full-waveform inversion in anisotropic media: An analytic parameter resolution study: Geophysics, **79**, R91–R101.

Bakulin, A., Grechka, V., and Tsvankin, I., 2000, Estimation of fracture parameters from reflection seismic data-part i: Hti model due to a single fracture set: Geophysics, **65**, 1788–1802.

Bansal, R., and Sen, M. K., 2010, Ray-born inversion for fracture parameters: Geophysical Journal International, **180**, 1274–1288.

Ben-Menahem, A., and Jr, R. L. G., 1990, Scattering of elastic waves by localized anisotropic inclusions: J. Acoust. Soc. Am., **87**, 2300–2309.

Ben-Menahem, A., Jr, R. L. G., and Sena, A. G., 1991, Green's tensor and radiation patterns of point sources in general anisotropic inhomogeneous elastic media: Geophysical Journal International, **107**, 297–309.

Ben-Menahem, A., and Singh, S., 1981, Seismic waves and sources: New York.

Brown, R. J., Lawton, D. C., and Cheadle, S. P., 1991, Scaled physical modeling of anisotropic wave propagation: Multioffset profiles over an orthorhombic medium: Geophysical Journal International, **107**, 693–702.

Calvet, M., Chevrot, S., and Souriau, A., 2006, P-wave propagation in transversely isotropic media i:finite-frequency theory: Physics of the Earth and Planetary Interiors, **156**, 12–20.

Chapman, C., 2004, Fundamentals of Seismic Wave Propagation: Cambridge University Express.

Chapman, C. H., and Coates, R. T., 1994, Generalized born scattering in anisotropic media: Wave Motion, **19**, 309–341.

Contreras, P., Grechka, V., and Tsvankin, I., 1999, Moveout inversion of p-wave data for horizontal isotropy: Geophysics, **64**, 1219–1229.

Dietrich, M., and Kormendi, F., 1990, Perturbation of plane-wave reflectivity of a depth-dependent elastic medium by weak inhomogeneities: Geophysical Journal International, **100**, 203–214.

Eaton, D. W., 1991, Seismic migration/inversion for transversely isotropic elastic media: Ph.D. thesis, The University of Calgary.

Gholami, Y., 2012, Two-dimensional seismic imaging of anisotropic media by full waveform inversion: Ph.D. thesis, UNIVERSITE DE NICE-SOPHIA ANTIPOLIS - UFR SCIENCES.

Gholami, Y., Brossier, R., Operto, S., Prieus, V., Ribodetti, A., and Virieux, J., 2013a, Which parameterization is suitable for acoustic vertical transverse isotropic full waveform inversion? part 2: Synthetic and real data case studies from valhall: Geophysics, **78**, R107–R124.

Gholami, Y., Brossier, R., Operto, S., Ribodetti, A., and Virieux, J., 2013b, Which parametrization for acoustic vti full waveform inversion? - part 1: sensitivity and trade-off analysis: Geophysics, **78**, R81–R105.

Gibson-Jr, R. L., 1991, Elastic wave propagation and scattering in anisotropic fractured media: Ph.D. thesis, Massachusetts Institute of Technology.

Hudson, J. A., 1980, Overall properties of a cracked solid: Math.Proc.Camb.Phil.Soc, **88**, 371–384.

Hudson, J. A., 1981, Wave speeds and attenuation of elastic waves in material containing cracks: Geophys.J.Roy.Astr.Soc, **64**, 133–150.

Innanen, K. A., 2014, Reconciling seismic avo and precritical reflection fwi? analysis of the inverse hessian: SEG Expanded Abstract.

Kamath, N., and Tsvankin, I., 2014, Sensitivity anaysis for elastic full-waveform inversion in vti media: SEG Expanded Abstracts, 1162–1166.

Karpfinger, F., M*ü*ller, T. M., and Gurevich, B., 2009, GreenâĂŹs functions and radiation patterns in poroelastic solids revisited: Geophysical Journal International, **178**, 327–337.

Liu, Q., and Tromp, J., 2006, Finite frequency kernels based on adjoint methods: Bulletin of the Seismological Society of America, **96**, 2383–2397.

Mahmoudian, F., 2013, Physical modeling and analysis of seismic data from a simulated fractured medium: Ph.D. thesis, The University of Calgary.

Musgrave, M. J. P., 1970, Crystal Acoustics: Holden-day.

Nelson, R. A., 1985, Geologic analysis of naturally fractured reservoirs: Golf Publishing Company, second edition edn.

Oh, J. W., and Min, D., 2014, Multi-parametric fwi using a new parameterisation for elastic vti media: EAGE Expanded Abstracts.

Operto, S., Gholami, Y., Ribodetti, A., Brossier, R., Metivier, L., and Virieux, J., 2013, A guided tour of multiparameter full waveform inversion with multicomponent data: from theory to practice: The Leading Edge, **32**, 1040–1054.

Pan, W., Innanen, K. A., and Margrave, G. F., 2014, A comparison of different scaling methods for least-squares migration/inversion: EAGE Expanded Abstract.

Plessix, R. E., and Cao, Q., 2011, A parametrization study for surface seismic full waveform inversion in an acoustic vertical transversely isotropic medium: Geophysical Journal International, **185**, 539–556.

Pratt, R. G., Shin, C., and Hicks, G. J., 1998, Gauss-newton and full newton methods in frequency-space seismic waveform inversion: Geophysical Journal International, **133**, 341–362.

Pujol, J., 2003, Elastic Wave Propagation and Generation in Seismology: Cambridge University Press.

Rüger, A., 1997, P-wave reflection coefficients for transversely isotropic models with vertical and horizontal axis of symmetry: Geophysics, **62**, 713–722.

Sato, H., and Fehler, M. C., 1997, Seismic Wave Propagation and Scattering in the Heterogeneous Earth: Springer.

Schoenberg, M., 1983, Reflection of elastic waves from periodically stratified media with interfacial slip: Geophysical Prospecting, **31**, 265–292.

Schoenberg, M., and Helbig, K., 1997, Orthorhombic media: Modeling elastic wave behavior in a vertically fractured earth: Geophysics, **62**, 1954–1974.

Shaw, K. R., and K.Sen, M., 2004, Born integral, stationary phase and linearized reflection coefficients in weak anisotropic media: Geophysical Journal International, **158**, 225–238.

Song, X., and Alkhalifah, T., 2013, Modeling of pseudo-acoustic p-waves in orthorhombic media with a lowrank approximation: Geophysics, **74**, C33–C40.

Stokes, G. G., 1851, On the dynamical theory of diffraction: Trans. Camb. Phil. Soc, **9**, 1–62.

Stolt, R. H., and Weglein, A. B., 2012, Seismic Imaging and Inversion: Application of Linear Inverse Theory: Cambriage University Press.

Tarantola, A., 1984, Inversion of seismic reflection data in the acoustic approximation: Geophysics, **49**, 1259–1266.

Tarantola, A., 1986, A strategy for nonlinear elastic inversion of seismic reflection data: Geophysics, **51**, 1893–1903.

Tarantola, A., and Valette, B., 1982, Generalized nonlinear inverse problems solved using the least square criterion: Rev. Geophys. Space Phys, **20**, 219–232.

Thomsen, L., 1986, Weak elastic anisotropy: Geophysics, **51**, 1954–1966.

Tromp, J. C., Tape, C., and Liu, Q., 2005, Seismic tomography, adjoint methods, time reversal and banana-doughnut kernels: Geophysical Journal International, **160**, 195–216.

Tsvankin, I., 1995, Body-wave radiation patterns and avo in transversely isotropic media: Geophysics, **60**, 1409–1425.

Tsvankin, I., 1997a, Anisotropic parameters and p-wave velocity for orthorhombic media: Geophysics, **62**, 1292–1309.

Tsvankin, I., 1997b, Reflection moveout and parameter estimation for horizontal transverse isotropy: Geophysics, **62**, 614–629.

Tsvankin, I., 2001, Seismic signatures and analysis of reflection coefficients in anisotropic media: ELSEVIER.

Tsvankin, I., and Chesnokov, E., 1990, Synthesis of body-wave seismograms from point sources in anisotropic media: Journal of Geophysical Research, **95**, 11,317–11,331.

Tsvankin, I., and Grechka, V., 2011, Seismology of azimuthally anisotropic media and seismic fracture characterization: SEG.

Vestrum, R. W., 1994, Group- and phase-velocity inversions for the general anisotropic stiffness tensor: Ph.D. thesis, The University of Calgary.

Virieux, A., and Operto, S., 2009, Inversion of seismic reflection data in the acoustic approximation: Geophysics, **74**, WCC1–WCC26.

Wild, P., and Crampin, S., 1991, The range of effects of azimuthal isotropy and eda ansiotropy in sedimentary basins: Geophysical Journal International, **107**, 513–529.

Wu, R., and Aki, K., 1985a, Elastic wave scattering by a random medium and the small scale inhomogeneities in the lithosphere: Journal of Geophysical Research, **90**, 10,261–10,273.

Wu, R., and Aki, K., 1985b, Scattering characteristics of elastic waves by elastic heterogeneity: Geophysics, **50**, 582–595.

Zheng, Y., Fang, X., Fehler, M. C., and Burns, D. R., 2013, Seismic characterization of fractured reservoirs by focusing gaussian beams: Geophysics, **78**, A23–A28.

Zhou, B., and Greenhalgh, S., 2009, On the computation of the fréchet derivatives for seismic waveform inversion in 3d general anisotropic, heterogeneous media: Geophysics, **74**, WB153–WB163.